Sequential drug treatment targeting cell cycle and cell fate regulatory programs blocks non-genetic cancer evolution in acute lymphoblastic leukemia

Alena Malyukova[1*†], Mari Lahnalampi[2†], Ton Falqués[3], Petri Pölönen[2], Mikko Sipola [2], Juha Mehtonen [2], Susanna Teppo[4], Johanna Viiliainen[1], Olli Lohi[4], Anna Hagström[3], Merja Heinäniemi[2*†], Olle Sangfelt[1*†]

1. Department of Cell and Molecular Biology, Karolinska Institutet, Stockholm, Sweden
2. The Institute of Biomedicine, School of Medicine, University of Eastern Finland, Kuopio, Finland
3. Division of Clinical Genetics, Department of Laboratory Medicine, Lund University, Lund, Sweden.
4. Tampere Center for Child, Adolescent and Maternal Health Research, Faculty of Medicine and Health Technology, Tampere University and Tays Cancer Center, Tampere University Hospital

† Equal contribution

* Corresponding authors

Olle Sangfelt,
olle.sangfelt@ki.se
Department of Cell and Molecular Biology, Karolinska Institutet, Biomedicum,
Solnavägen 9, 171 77, Stockholm, Sweden
Alena Malyukova,
aljona.maljukova@ki.se
Department of Cell and Molecular Biology, Karolinska Institutet, Biomedicum,
Solnavägen 9, 171 77, Stockholm, Sweden
Merja Heinäniemi
merja.heinaniemi@uef.fi
The Institute of Biomedicine, University of Eastern Finland

Running Title: WEE1 is a precision medicine target in B-ALL

Key Words: single cell multiomics, WEE1, AZD1775, RUNX1, KMT2A-r, pre-BCR, BCL6 B-ALL, leukemia, chromatin state, cell state transition

ABSTRACT

Targeted therapies exploiting vulnerabilities of cancer cells hold promise for improving patient outcome and reducing side effects of chemotherapy. Yet, mechanistic understanding linking drug effects and cancer cell state diversity is crucial for identifying effective combination therapies to prevent disease recurrence.

Here, we characterized at the level of gene regulatory networks the effect of G2/M cell cycle checkpoint inhibition in acute lymphoblastic leukemia (ALL) and demonstrate that WEE1 targeted therapy impinges on cell fate regulatory circuits. We found highest inhibition of recovery of proliferation in KMT2A-rearranged (KMT2A-r) ALL cells, compared to other leukemia subgroups. Single-cell transcriptome and chromatin accessibility profiling of (*KMT2A*::*AFF1*) RS4;11 cells treated with AZD1775 revealed strong activation of p53-driven processes linked to induction of apoptosis and senescence, and disruption of a core KMT2A-RUNX1-MYC regulatory network through CDK1-mediated RUNX1 degradation. In RS4;11 cells and in patient-derived xenograft (PDX) model, we uncovered that a transition to a cell state characterized by activation of transcription factors regulating pre-B cell fate, lipid metabolism and pre-BCR signaling supported a drug tolerance. By sequential treatment targeting the drug tolerant cell state phenotype with BCR-signaling inhibitors dasatinib, ibrutinib, or perturbing metabolism by fatostatin or AZD2014 after AZD1775 administration, this cell state evolution underlying recovery of leukemic cells could be blocked. Collectively, our findings provide new insights into the tight connectivity of gene regulatory programs associated with cell cycle and cell fate regulation, and a rationale for sequential administration of WEE1 inhibitors with low toxicity inhibitors of pre-BCR signaling or metabolism.

INTRODUCTION

The WEE1 checkpoint kinase is a key regulator of the G2/M and G1/S transitions during cell division cycle (Moiseeva, Qian et al. 2019) (Elbaek, Petrosius et al. 2022) through inhibitory phosphorylation of cyclin-dependent kinases 1/2 (CDK1/2) (Parker, Sylvestre et al. 1995), (Watanabe, Arai et al. 2005). WEE1 supports genome integrity by suppressing excessive origin firing during DNA replication and premature entry into mitosis (Russell and Nurse 1987), (McGowan and Russell 1995), (Sorensen and Syljuasen 2012). Consequently, inhibition of WEE1 removes the negative phosphorylation on CDK1/2 (in concert with CDC25) resulting in deregulation of CDKs, increased origin firing and replication fork degradation leading to fork collapse, DNA damage and unscheduled mitosis (Hirai, Iwasawa et al. 2009)(Mahajan and Mahajan 2013)(Moiseeva, Qian et al. 2019)(Petrosius, Benada et al. 2023). Recent studies show that WEE1 inhibition by AZD1775 (Adavosertib), a potent and specific small-molecule inhibitor, alone or in combination with DNA damaging agents effectively kills cancer cells of various origins (Hirai, Iwasawa et al. 2009), (Carrassa and Damia 2017), (de Jong, Langendonk et al. 2019). The targeting of DNA damage response-related proteins while also challenging the cell with genotoxic agents is a widely adopted concept in cancer therapy (O'Connor 2015). However, clinical application is restrained by a high rate of toxicity in combination with chemotherapy (O'Connor 2015)(Kong and Mehanna 2021)(Fu, Wang et al. 2018) (Takebe, Coyne et al. 2018).

Acute lymphoblastic leukemia (ALL) is the most common type of childhood cancer, typically of B-cell lineage. Approximately 75% of B-ALL cases contain chromosomal rearrangements involving alteration of lineage specific transcription factors (TFs) that are critical regulators of B-cell development and serve as prognostic markers underlying clinical responses. Mixed lineage leukemia (MLL) refers to chromosomal translocations involving the gene *KMT2A*

which encodes histone lysine N-methyltransferase 2, an important regulator of epigenetic maintenance of stem cell gene transcription through activating histone modification at target genomic loci (Chan and Chen 2019). Despite improved treatment protocols with higher response rates and better outcomes for children with ALL, KMT2A-r patients respond poorly to conventional chemotherapy (Liedtke and Cleary 2009, Winters and Bernt 2017). However, these leukemias typically harbor very few additional mutations that could underlie drug resistance (Andersson, Ma et al. 2015). Recently, single cell genomics-approaches have provided new insight into the aberrant gene regulatory programs and non-genetic drug resistance mechanisms in leukemia (Knoechel, Roderick et al. 2014, Mehtonen, Teppo et al. 2020,(Chen, Yu et al. 2022). A network of regulatory interactions exerted by TFs underlies persistent cell phenotypes. Increased drug tolerance in leukemia is often attributed to "stemness" properties, due to shift into more immature (stem-like) states - a phenotype switch governed by gene regulatory networks as opposed to resulting from genomic mutations (Ebinger, Ozdemir et al. 2016, van Galen, Hovestadt et al. 2019, Khabirova, Jardine et al. 2022,(Chen, Yu et al. 2022).

Chromosomal rearrangements of the *KMT2A* gene can produce many different chimeric TFs through in-frame fusions with various partner genes (Meyer, Kowarz et al. 2009), in ALL most commonly resulting in KMT2A::AFF1 (AF4) and KMT2A::ENL fusions through t(4;11) and t(11;19) rearrangements, respectively. These fusion proteins lack the C-terminal SET domain which normally confers the KMT2A multiprotein complex histone H3K4 methyltransferase activity. KMT2A fusion proteins instead associate with the super elongation complex, resulting in a differentiation arrest at the early hematopoietic progenitor state due to increased levels of activating H3K79 methylation by DOT1L at genomic loci such as *HOXA9* and *MEIS1*, which

are associated with leukemic transformation (Okada, Feng et al. 2005) (Winters and Bernt 2017). However, KMT2A fusions also compromise the S-phase checkpoint by abrogating stabilization of wild-type KMT2A upon DNA damage, thereby preventing trimethylation of H3K4 and causing aberrant loading of CDC45 at late replication origins (Liu, Takeda et al. 2010). Recent work further indicates that other hematopoietic master regulators of stemness and development, notably RUNX proteins, also participate in cell cycle checkpoint control and DNA repair independent of their transcription activities (Wilkinson, Ballabio et al. 2013, Wray, Deltcheva et al. 2022, Friedman 2009, Tay, Krishnan et al. 2018). The aberrant impact of KMT2A fusion proteins at the convergence of two pivotal regulatory pathways, cell cycle checkpoint and cell fate control, represents a potential vulnerability; however, whether it can be targeted for therapy for leukemia treatment has not been explored.

Cancer cell responses to drug perturbations are often assayed using simple phenotypic readouts, such as proliferation or cell death. However, these end-point assays are insufficient to uncover potential cellular mechanisms that allow some cells to survive. Moreover, distinguishing between selection of pre-existing drug resistant cells and acquired drug tolerance through drug-induced adaptive mechanisms is important to predict long-term drug efficacy. In the present study, we characterize in detail the genome-wide response and cell state evolution upon cell cycle checkpoint-targeted therapy in leukemic cells through single cell multi-omics and demonstrate that perturbing the cell cycle regulation directly impacts cell fate regulatory circuits that can underlie a transition to a drug-tolerant cell phenotype. Contrary to currently held view that the stemness features attributed to KMT2A-leukemias critically underlie drug resistance, upon targeting the cell cycle control vulnerability of KMT2A-r leukemias, the drug-tolerant cells corresponded to a more differentiated phenotype with expression of pre-BCR and

BCL6. We show that WEE1 inhibition followed sequentially by drugs targeting the persisting cell state regulatory program prevents recovery in KMT2A-r and pre-BCR+ ALL cells, while no synergy was seen in concurrent drug schedule.

RESULTS

WEE1 inhibitor AZD1775 results in prolonged growth-inhibition selectively in KMT2A-r B-ALLs

WEE1 expression was previously reported to be higher in primary ALL blasts compared to normal mononuclear cells (Ghelli Luserna Di Rora, Beeharry et al. 2018). To determine whether specific leukemia subtypes may rely more on *WEE1* expression, we used our data resource Hemap (http://hemap.uta.fi/) with curated genome-wide transcriptomic data from more than 30 hematologic malignancies. Interestingly, *WEE1* expression was significantly higher (adjusted p-value <0.01, Wilcoxon test) in the KMT2A-r ALL subtype (Figure 1A, see also Figure S1A comparing KMT2A::AFF1, KMT2A::MLLT1 and KMT2A::MLLT3). Higher *WEE1* expression in KMT2A-r compared to other ALL subtypes raised the possibility that KMT2A-r cells may be more vulnerable to targeted inhibition of the WEE1 kinase. However, since WEE1 activity is regulated also at protein level via phosphorylation, we performed further functional evaluation comparing different leukemic cell lines. First, to assess sensitivity of leukemic cells that represent different ALL subtypes and lymphoid lineage differentiation states to WEE1 kinase inhibition, we treated a panel of 15 ALL cell lines with increasing concentrations of AZD1775 (Figure 1B). Acute drug treatment induced apoptosis as measured by activation of caspase-3/7, and reduced cell viability in a dose-dependent manner in all cell lines (Figure 1B, Figure S1B).

Next, we assessed whether the response to AZD1775 persisted, by measuring recovery of proliferation post-treatment in leukemia cell lines, comparing the different chromosomal

translocations, including *ETV6-PDGFRB* (Nalm-6), *TCF3-PBX1* (697, RCH-ACV and Kasumi-2), *ETV6/RUNX1* (REH) and KMT2Ar-ALLs (RS4;11, SEM, ALL-PO and KOPN8). Cells were treated with AZD1775 at sublethal dose (GI50 concentration) for three days followed by drug washout and regrowth in drug-free media. Although acute response to AZD1775 (GI50) did not associate with any specific ALL subtype (Figure S1B), WEE1 inhibition markedly attenuated re-proliferation following drug washout of KMT2A-r cells as opposed to non-KMT2A-r cells (Figure 1C, Figure S1D). Thus, the KMT2A-r subtype with the highest expression of *WEE1* exhibits significantly reduced recovery, in line with the patient genomics cohort (Figure 1A) result. To provide independent cell line evidence based on Crispr-Cas9 targeting across haematopoietic malignancies, we further analyzed *WEE1* gene dependency scores using DepMap portal (https://depmap.org/portal/) and found a greater dependency on WEE1 in leukemia cell lines with higher *WEE1* expression (Spearman r = -0.336, Figure S1C). However, characterization of the response to AZD1775 monotherapy cycles *in vivo*, using a primary KMT2A-r patient-derived xenograft (PDX) model MLL-7 (*KMT2A::AFF1*) in (Richmond, Carol et al. 2015) NOD.Cg-*PrkdcscidIl2rgtm1Wjl*/SzJ (NSG) mice (N=3 per group) transplanted with leukemic cells did not indicate a strong survival benefit (Figure 1D, AZD1775 median survival; 44 days, DMSO median survival; 42 days, see also Figure S1E-I), warranting a therapy strategy informed by cellular properties that contribute to drug tolerance.

To explore the molecular determinants of the AZD1775 response, we selected KMT2A-r RS4;11 cells and non-MLL-r Nalm-6 cells for more in-depth analysis. First, we confirmed that AZD1775 reduced phosphorylation of CDK1 on threonine 15, increased PARP cleavage and triggered DNA damage rapidly, as measured by phosphorylation of γH2AX (Figure 1E, RS4;11 cells), according to the established mode of action of AZD1775. To confirm that RS4;11 cells treated with AZD1775 enter G2/M prematurely, cells were pulse-labelled with EdU and treated

with DMSO or AZD1775 for different times, up to 32 hours. As shown in Figure 1F, while DMSO-treated cells divided and re-entered G1-phase, a large proportion of AZD1775 treated RS4;11 cells stalled at G2/M and failed to proceed through the cell cycle.

Since the KMT2A-r cell lines tested retain the KMT2A-fusion and represent a genetically homogenous clonal origin, we hypothesized that drug resistance in the recovering cells could derive from a pre-existing drug-tolerant cell population or become acquired through cell state transition driven by TF activity changes whereby a fraction of cells is able to adapt and accommodate a new phenotypic state that support drug tolerance. To distinguish between these, we used the RS4;11 cells as cellular model system (Figure 1G). We performed global run-on sequencing (GRO-seq) to assess early effects on newly synthesized RNA at gene and enhancer regions at 4, 10 and 24 hours. The 10 and 24 h time points were then further resolved using single cell RNA (scRNA)- and ATAC (scATAC)-sequencing to address the underlying cell state heterogeneity both at the level of transcription and chromatin access. We then used the combination of these assays to inform about the presence of drug-tolerant cell states, association between early transcriptional changes, chromatin access and regulatory network activities (Figure 1G).

WEE1 kinase inhibition triggers a rapid transcriptional response and emergence of multiple cell states

The time course GRO-seq profiles identified 1239 significant gene transcription changes comparing across time points (F-test adjusted p-value < 0.001). The temporal response to AZD1775 in bulk (Figure 2A) could distinguish: 1) genes primarily upregulated at 4 hours, exemplified by the GRO-seq signal at the *PLK1* gene locus (Figure 2B), 2) genes peaking in upregulation at 10 hours, 3) genes most strongly upregulated at 24 hours, and 4) genes downregulated at all time points (see also Table S1). Pathway enrichment analysis revealed

genes associated with regulation of the cell cycle, DNA replication, PLK1/AURORA signaling, FOXM1 transcription factor network and M-phase pathways in the early (4 h) upregulated cluster (Figure 2C). Genes functionally related to cell cycle checkpoints, DNA-strand elongation, activation of pre-replication complexes and S-phase were repressed in the bulk genomics data (Figure 2A bottom, “down”).

Since the WEE1 inhibition interferes with a central decision point of cell fate control during cell cycle, we anticipated that this perturbation would result in cells occupying distinct states. To expose the diversification and nature of responses of individual cells we therefore performed single-cell transcriptome and chromatin access measurements. scRNA-sequencing revealed that 24 h after treatment with AZD1775, the surviving cells analyzed alongside DMSO treated cells formed 11 discernable cell clusters (Figure 2D). We refer to these clusters as cell states hereafter. As determined by expression of cell cycle phase specific markers, the clusters 2, 3 and 4, correspond to different cell cycle phases present in DMSO-treated cells. The other clusters, 5-11, were almost completely represented by AZD1775 treated cells (Figure 2E). As noted in the bulk GRO-seq analysis, treated and surviving cells had reduced number of cells in the transcriptional state associated with S phase and an enrichment of cells in G1 or G2/M phase (Figure 2F), indicating an arrest at the G1/S checkpoint and a possible failure to progress through mitosis, consistent with the flow cytometry data of Figure 1F.

Since the bulk GRO analysis indicated ongoing transition and possible adaptation of cells arising already at 10 h, we performed single-cell RNA- and ATAC-seq assayed in parallel from the same cells based on the multiome protocol to examine how open chromatin sites impact the transcriptional response and cell state diversity at single-cell resolution at 10h of treatment, and also compared the cell states to the scATAC-seq profile acquired at 24 h.

First, to investigate the correspondence between cell states identified from the single cell transcriptome and clustering of cells defined by their chromatin access, we examined the transcriptome and chromatin dynamics by separating the cells by treatment from 10 and 24 h (Figure 2G, Figure S2). Matching cell clustering could be distinguished from the separate clustering of multiome scRNA- and scATAC-seq data and between the 10 and 24 h time points (transcriptome-based cell state labels are shown, see also Figure S2B-G).

Secondly, we contrasted the alternative scenarios of differential survival of pre-existing cell states and emergence of treatment-induced cell states. The predominant cell state dynamics (Figure 2G left) in DMSO treated cells matched to active cell cycle transitions, as indicated by lines on the UMAP based on RNA velocity and PAGA graph analysis (see Methods). By contrast, AZD1775 treated cells at 10 and 24 h (Figure 2G, middle and right, respectively) followed a trajectory along three distinct branches. The first branch is dominated by cell state 11 (cell fate I), a second branch corresponds to a succession of cell states from 5 to 7 (cell fate II), and a third small population of cells branch to cell state 9 (cell fate III) (Figure 2G), each trajectory being unique to AZD1775 treated cells.

Altogether, despite the highly heterogeneous response, we found high concordance between the cell subpopulations analyzed using both RNA- and ATAC-seq analysis, and between bulk and single cell pathway analyses. This initial analysis supports the scenario that AZD1775 treatment could impact the gene regulatory network, leading to the emergence of new cell states with unique active transcription profiles. Next, we proceeded to elucidate whether this grouping based on the transcriptome and chromatin dynamics indeed reflects functional cell fates based on additional analyses.

Forced mitotic entry in response to AZD1775 treatment arrests cells from S-phase in a condensed mitotic-like chromatin state

Cell state 11 distinguished a distinct subpopulation (cell fate I) that was evident already after 10 h and persisted at 24 h of AZD1775 treatment (Figure 2G middle and right, respectively). Based on scATAC-seq TF motif analysis, these cells had elevated S-phase (E2Fs, YY1, Table S3) and mitotic checkpoint (NRF1, Ronin, Sp1) TF motif access (Figure 3A and Figure S3A,B). Simultaneously, these cells showed evidence of mitotic entry downstream the forced activation of CDK1 based on the scATAC-seq fragment length distribution, with cells corresponding to cell fate I exhibiting a condensed chromatin state and elevated nucleosome signal metric (Figure 3B, see also Figure S3C,D). Moreover, pathway enrichment from scRNA-seq cell cycle phase marker genes was consistent with a mitotic-like state (Figure S2H and Table S2). Premature entry into mitosis can extend mitosis and enhance cell death (Visconti, Della Monica et al. 2015). In agreement with delayed mitotic exit, the fraction of phosphorylated serine 10 histone 3 (pS10-H3) with 4N DNA content increased with treatment time, reflecting a mitotic-like arrest (Figure 3C).

We also performed scRNA-seq in non-KMT2A-r Nalm-6 cells for comparison. In sharp contrast to RS4;11, the majority of AZD1775 treated Nalm-6 cells retained a population in the active cell cycle (matched to cell states 2-4), in line with their ability to rapidly recover and proliferate upon drug withdrawal (Figure S3E). Accordingly, phosphorylation of S10-H3 was only transiently increased in Nalm-6 cells, while it was continuously high in RS4;11 cells treated with AZD1775 (Figure S3F), supporting a reduced capacity of KMT2A-r cells to cope with AZD1775-driven CDK-activation and replication stress compared to non-KMTA2-r cells.

AZD1775 triggers unscheduled replication characterized by genome-wide p53 response

Comparison of the other cell clusters detected from scATAC-seq (referred to as “chromatin states”) revealed that AZD1775-induced genome-wide changes in chromatin access with

overall highly distinct TF motif access patterns (Figure 4A) that could underlie the emergence of distinct cell fates upon replication stress.

Elevated access at binding motifs for p53 (and bZIP-factors JUN/AP, FOS, Atf) was characteristic of AZD1775-specific chromatin states 1 and 2 (Figure 4B). As can be seen from the TF motif access score visualized on the scRNA-seq map (Figure 4C), these cells corresponded to the branch leading to cell states 6-7 on the scRNA-seq map (cell fate II) (Figure 4C).

Based on the scATAC-seq profiles of the distinct cell states, the elevated p53 TF motif access (Figure 4A, in pattern 1) anti-correlated with two other TF motif access patterns (Figure 4A, patterns 2 and 3). Closer inspection of pattern 2 revealed mutual exclusivity with the lymphoid progenitor TF RUNX1 (clustered together with bHLH motifs recognized e.g. by AP4) (Figure 4B, Figure S5A). RUNX1 is a key TF regulating target genes downstream of KMT2A-AFF1 in a feedforward loop (Harman, Thorne et al. 2021) and was expressed at higher levels in KMT2A-r patients compared to other ALL subtypes (Figure S5A). To further explore the relationship between cell state-specific chromatin accessibility and transcriptional regulation, we visualized the scATAC-seq signal profile at enhancer regions with highest or lowest chromatin access in chromatin state 1 (Figure 4D, AZD1775-treatment). Next, we generated RUNX1 ChIP-seq profile from RS4;11 cells (basal state) and retrieved p53 ChIP-seq signals from doxorubicin stimulated lymphoblastoid cells (Figure 4E). The average TF occupancy signals at these cell fate II-specific high chromatin access regions showed high p53 and low RUNX1 signal, while an opposite profile characterized the low access regions, providing further confirmation of their mutually exclusive TF activities. Notably, cells with high RUNX1 TF motif activity in AZD1775-treated cells (chromatin states 4 and 5) corresponded to transcriptome cell states 1-4 (present also at basal state), that in relative cell proportion decreased from 60% at 10 h to 11% at 24 h.

To further explore the relationship between cell state-specific chromatin accessibility and transcriptional regulation, we quantified transcription from enhancers (enhancer RNA, eRNA) at these same regions (AZD1775, chromatin state 1). This regulatory region activity profile showed that enhancers in cell fate II-specific accessible chromatin were transcriptionally silent at 4 and 10 h (Figure 4F). This is in agreement with gene-level GRO-seq results that indicated delayed upregulation of the p53-signaling network and pathways regulating apoptosis (cluster active at 24 h, Figure 2A). Enrichment of p53 and bZIP binding motifs in enhancer regions active at 24 h was independently validated in the bulk GRO-seq data (see Methods, Figure 4G Figure S4D, Table S4). Hence, inducing a p53 response from initially silent regulatory regions could allow cells time to adapt and initiate pro-survival responses.

CDK-mediated degradation results in loss of RUNX1 in response to AZD1775

To further characterize the decline in RUNX1 activity and other pattern 2 TFs, including the KMT2A::AFF1 TF target MYC that promotes leukemia survival (Harman, Thorne et al. 2021), we performed immunoblot analysis (in bulk) and found that AZD1775 treatment decreased RUNX1 protein expression levels in KMT2A-r RS4;11 and SEM cells, and in several non-KMT2A-r ALL cell lines (Figure 5A, Figure S5B). The hematopoietic stem cell TF GATA2 and MYC similarly had declining protein expression following AZD1775 treatment (Figure S5D-E). In comparison, ATF4 that acts as transcriptional activator of the integrated stress response was transiently induced at 4 h (Figure S5C).

RUNX1 was previously reported to be degraded in a CDK-dependent manner by the APC ubiquitin ligase complex during mitosis (Biggs, Zhang et al. 2005, Wang, Zhang et al. 2007). Based on the scATAC-seq TF motif analysis in DMSO-treated cells, the RUNX1 and bHLH motifs have the highest access at G1 and lowest access in G2 (Figure S5D, see also Figure S2C). We hypothesized that without the inhibitory phosphorylation by WEE1 (AZD1775

treatment), hyperactivation of CDK1/2 may promote ubiquitination and proteasomal degradation of RUNX1 during G2/M. Supporting this, AZD1775 treatment did not alter *RUNX1* mRNA expression levels in RS4;11 cells or in other B-ALL cell lines (Figure S5E), but increased RUNX1 protein ubiquitination upon proteasomal inhibition (Figure 5B). We next verified that RUNX1 levels decreased following release from a G2/M-phase block as compared to cells released from a G1/S-phase block (Figure 5C). Concurrent treatment with the CDK1 inhibitor RO3306 and AZD1775 partially rescued downregulation of RUNX1 protein, and reduced PARP cleavage and γH2AX (Figure 5D), further supporting CDK1-driven ubiquitination and proteasomal degradation of RUNX1 in response to WEE1 inhibition (illustrated in Figure 5E).

Together, these results suggest that WEE1 inhibition may interrupt a core KMT2A-r transcriptional regulatory program involving RUNX1-MYC-GATA TFs through reduced protein expression.

Stress- and pre-B-state regulatory programs distinguish a drug-tolerant sub-population with pre-BCR and BCL6 gene loci activation

Functionally, RUNX1 is part of a core regulatory circuit that acts as a switch, governing cell fate commitment (Harman, Thorne et al. 2021). Consequently, perturbing RUNX1 expression and TF activity dynamics by WEE1 inhibition may induce a transition to an alternative cell state. In line with this, the cell fate III subpopulation (cell state 9, Figure 2G) had decreased RUNX1 motif activity (Figure 4A, AZD chromatin state 3), but significantly higher chromatin access of pre-B cell state TF motifs, including PAX5, EBF, GR and MEF2C, and high motif activity of TFs regulating cellular metabolism (SREBF, THR, LXR) (Figure 6A, see also Figure S6A-B). As a distinct feature, cell state 9 (cell fate III)-specific open chromatin regions had highest NfKB and heat shock factor (HSF) motif access (Figure 6A). Supporting activation of

a functional TF circuitry, cell fate III cells had high expression of the respective TF target genes regulating lipid metabolism (*LDLR*, *HMGCS1*), HSF (*HSPA1B*), GR (*TSC22D3*), NFkB (gene set activity) and pre-BCR signaling (*BCL6, SOCS1)* (Figure S6C-E, Table S2). The combination of stress- and pre-B fate specific TF activation pointed towards the initiation of an adaptive cell state transition in response to AZD1775 treatment. In a similar fashion, we quantified enhancer regions that represent highest vs lowest sc-ATAC-seq signal in cell fate III (AZ chromatin cluster 3) and compared chromatin access (Figure 6B, scATAC-seq signal) and enhancer activity (Figure 6C, GRO-seq signal). Interestingly, the regions with high access in cell fate III were transcribed, although at low level, also in basal state (grey lines, Figure 6C), indicative of a primed state. Upon AZD1775 treatment, these enhancers were rapidly further activated (4 and 10 h profiles in red, Figure 6C). Comparison to NfKB ChIP-seq signal in lymphoblastoid cells provided further confirmation that the chromatin regions in cell fate III-specific open chromatin harbor NFkB binding sites (Figure 6D, upper panel). In comparison, the ChIP-seq signal at enhancers with lowest chromatin access revealed that these sites were p53-bound in lymphoblastoid cells treated with doxorubicin (Figure 6D, lower panel), which could indicate active suppression of p53 chromatin recruitment in cell fate III. Moreover, chromatin access was increased at gene loci encoding *MEF2D, SREBF1, BCL6, SOCS1* and pre-BCR signaling pathway components that are central to cellular survival pathways in B-lymphoid cells (Figure 6E), resembling a previously recognized leukemia-associated TF circuitry active in MEF2-fusion subtype of ALL (Tsuzuki, Yasuda et al. 2020).

To investigate whether the emergence of cell fate III constitutes a potential escape mechanism and drug-tolerant cell state linked to recovery following AZD1775 treatment, we analysed pre-BCR and BCL6 protein expression in cells treated with AZD1775 for 72 h, and after 10 days of recovery. Notably, the drug tolerant cells that persisted at 72 h matched the pre-BCR+/BCL6+ population (cell fate III). At 72 h, pre-BCR levels were strongly upregulated in

RS4;11 cells (Figure 6F top panel). This activation occurred in a reversible manner, as pre-BCR expression was restored to basal levels after 10 days recovery (Figure 6G). By contrast, BCL6 protein levels increased at 72 hours and the expression persisted for 10 days (Figure 6F,G).

Based on the data obtained, we hypothesized that leukemic cells that can readily adopt the BCL6+pre-BCR+ cell state may have higher tolerance to AZD1775. The difference in the temporal dynamics of transcriptional activation of cell state II vs cell state III enhancers observed in RS4;11 cells, together with the lower chromatin access at p53 binding sites could increase drug tolerance in cell fate III. The Nalm-6 cells used as comparison represent a pre-BCR+ leukemia and accordingly, showed a much smaller cell cluster matching p53 regulated gene sets (Figure S4E, scRNAseq profile of AZD1775 treated Nalm-6 cells). In addition, the activation of caspase 3/7 was higher in KMT2A-r cells compared to non-KMT2A-r cells (Figure S6E, left). Since p53 also modulates the senescence program in response to replication stress, we also quantified senescence following AZD1775 treatment. Indeed, we found an increased proportion of SA-β-Gal-positive cells in AZD1775 treated KMT2A-r compared to non-KMT2A-r cell lines (Figure S6F, right), congruent with increased expression of double-stranded DNA (dsDNA) sensor pathway (*cGAS*, *STING*) and components of the senescence-associated secretory pathway (SASP, *HMGB2*) in RS4;11 cells (Figure S4F-G) and high gene set score for senescence pathway (Figure S6G). Taken together, these data demonstrate a higher drug tolerance of pre-BCR+BCL6+ cells (cell fate III).

Sequential drug treatment can target non-genetic evolution of leukemic cells

To examine the candidate cell state markers for drug tolerance (Figure 6) in primary KMT2A-r cells, we analyzed the early transcriptional changes to single-agent AZD1775 treatment in the MLL-7 PDX model. Cells were collected for scRNA-seq after 28 h treatment with 120 mg/kg AZD1775 or vehicle and sorted for alive $CD45^{+}CD19^{+}$ population (Figure S7A-B). Among the

seven identified cell clusters (Figure 7A, refer also to Figure S7B), gene enrichment analysis revealed significant over-representation of genes from the BCR signaling pathway in the smallest cluster (cluster 6, Table S2). Resembling the profile found in RS4;11 cell state 9, expression of pre-BCR or BCR signaling and pre-B TF genes was increased, while *MYC* levels declined in this cluster (Figure 7A). Previous work established that MEF2D, SREBF1 and BCL6 create a functional TF circuit in MEF2D-fusion ALL (Tsuzuki, Yasuda et al. 2020). Therefore, we included an *in vivo* treatment profile in a MEF2D-fusion ALL case for comparison (Figure 7B). The tightly coordinated expression of *MEF2D*, *BCL6* and *SREBF1* and several BCR-signaling genes further supports that this transcriptional circuit is activated upon drug-induced stress and that the tolerant cell phenotype is present *in vivo* in primary KMT2A-r and in MEF2D-fusion patient ALL cells (Figure 7A-B).

Drugs disrupting this regulatory network activated in cell fate III could have high efficacy in preventing recovery of the remaining leukemic cell population. Therefore, we selected drugs that target pre-BCR signaling (dasatinib and ibrutinib) (Bicocca, Chang et al. 2012) (Kim, Hurtz et al. 2017) and based on higher TF access observed in cell state III for master regulators of cellular lipid metabolism such as SREBF1, included also inhibitors of metabolism (mTOR inhibitor AZD2014) and fatty acid synthesis (fatostatin) (Kamisuki, Mao et al. 2009, Basu, Dean et al. 2015). To assess the potential of repositioning these drugs as effective combination therapies with AZD1775, we first measured efficacy of each drug as single agents in a drug washout setting (illustrated in Figure 7C-D, Figure S7C) and quantified the ability of cells to recover as this experimental setup better mirrors the ability of drug-tolerant cells to recover post-treatment. As monotherapies, these drugs did not affect recovery of proliferation, and interestingly (Figure S7C), nor when administered concurrently in combination with AZD1775 (Figure 7C). Supporting successful targeting of adaptive survival pathways, the sequential administration of AZD1775 with the tested drugs effectively prevented cell survival

of KMT2A-r RS4;11 and ALL-PO cells (Figure 7D). Notably, administration of AZD1775 followed by AZD2014, dasatinib or ibrutinib also strongly attenuated recovery of non-KMT2A-r Nalm-6 cells (Figure 7D).

Taken together, these results show that perturbing cell cycle regulation through inhibition of WEE1 kinase in KMT2A-r cells triggers multiple distinct genome-wide responses that include rewiring of TF programs. Sequential administration of AZD1775 with drugs targeting metabolism and pre-BCR signaling can disrupt the non-genetic evolution to drug resistant state, thus providing new opportunities for drug repositioning in preventing leukemic cell recovery (Figure 7E).

Discussion

Targeted therapy holds promise in cancer treatment to reduce the toxicity of long-term chemotherapy. However, the acquisition of cancer cell phenotypic changes driven by tolerance pathways and emergence of acquired resistance is a common drug escape mechanism that occurs in various cancer types in response to a range of targeted treatments. In the present study, we characterized in detail the genome-wide response and cell state evolution upon cell cycle checkpoint-targeted therapy through inhibition of WEE1 kinase in ALL. Data-driven analysis from the HEMAP and the DepMap genomics resources combined with drug response profiling in different ALL subtypes revealed higher expression and increased WEE1 gene dependency in KMT2A-r compared to other subtypes. We show that WEE1 inhibition and CDK1 activation led to degradation of RUNX1 and that protein levels of other key TFs regulating the KMT2A-r leukemic phenotype were decreased. By comprehensively profiling the drug response dynamics using primary transcription and single cell transcriptome and chromatin readouts at different time points, we demonstrate that a more drug tolerant cell state was induced in surviving cells through a TF network upstream pre-BCR and BCR signaling genes. We

confirmed that this drug-tolerant cell state was present in a primary KMT2A-r patient-derived xenograft model and resembled a TF circuit found in MEF2D-fusion positive ALL. The systematic characterization of the drug response at the regulatory network level afforded an opportunity to design specific drug combinations that when administered sequentially with WEE1 inhibitor prevented recovery in ALL cells.

Upon WEE1 inhibition, most of ALL cell lines, including KMT2A-r cells, rapidly enriched for cell cycle markers consistent with deregulated DNA replication and unscheduled transition into G2M-phase, leading to cell death. Yet, at transcriptional and epigenetic level, already after 10 h treatment, three distinct cell fates emerged in response to AZD1775 exposure: I) a condensed chromatin and extended mitotic arrest, II) strong p53 activation leading to induction of apoptosis and senescence pathways and importantly, III) switch to drug tolerant cell state with higher chromatin access at TF motifs of NfKB, MEF2D and the metabolic regulators SREBF and LXR, a TF circuit regulating highly correlated expression of BCL6 and pre-BCR genes. Based on the single cell assays, ATAC DNA fragmentation pattern and primary transcription activity, these cell states were defined by unique gene transcription and chromatin access and were not present under basal conditions in RS4;11 cells. In comparison, pre-BCR+ MEF2D ALL was previously reported to depend on a similar TF circuit (Tsuzuki, Yasuda et al. 2020) that we identified in this study as the induced drug-tolerant cell state in KMT2A-r ALL.

As revealed by pulse-chase labeling of replicating cells, AZD1775 promoted premature entry into mitosis from S-phase. The condensed chromatin state (cell fate I), also visible in scATAC-seq, remained unresolved still at 32 h, consistent with delayed mitotic exit. The comparison of enhancer activation signals in the cell fate-specific open chromatin at p53, RUNX1 and NFkB bound sites provided insight into how the alternative cell fates could arise downstream TF activity changes: a progressive response activating p53-bound sites in cell fate II diverted cells with unscheduled S-phase entry away from cell cycle and towards cell death and senescence

through p53 activation at initially transcriptionally silent regions. Delayed mitotic exit and replication stress response are consistent with previously recognized drug mechanism of action (Elbaek, Petrosius et al. 2020) (Moiseeva, Qian et al. 2019). However, loss of chromatin access at RUNX1 occupied sites and activation of cell fate III-specific chromatin co-localizing with NFkB sites represent a previously unrecognized connection between cell cycle and cell fate regulatory circuits.

Remarkably, the p53-driven response anti-correlated with TFs that participate in the core KMT2A-r gene regulatory network, including RUNX1, GATA2 and MYC (Cai, Gao et al. 2015, Harman, Thorne et al. 2021). Both MYC and RUNX1 are crucial drivers of leukemogenesis and regulatory targets of KMT2A-r fusions (Guenther, Lawton et al. 2008, Wilkinson, Ballabio et al. 2013) and in particular KMT2A-r cells display strong addiction to RUNX1 for survival (Wilkinson, Ballabio et al. 2013, Wray, Deltcheva et al. 2022). The loss of RUNX1 through protein degradation may impinge upon multiple surveillance mechanisms that when disrupted enhance the sensitivity of KMT2A-r cells to AZD1775. RUNX proteins have been reported to function directly as integral regulators of DNA repair via the Fanconi Anemia pathway (Tay, Krishnan et al. 2018), while previous studies demonstrated that KMT2A-r cells have compromised the ATR-mediated S/G2-phase checkpoint (Liu, Takeda et al. 2010). Consequently, inhibition of WEE1 in KTM2A-r cells may not only override the G2/M-phase checkpoint but also cause disruption of the G1/S checkpoint (Moiseeva, Qian et al. 2019), resulting in CDK1/2-driven unscheduled origin firing, p53 activation and senescence/apoptosis. Accordingly, the critical function of WEE1 kinase in cell cycle/checkpoint regulation and increased dependency on RUNX1 in KMT2A-r is underscored by the predominant cell fates associated with apoptotic or senescent states in this subtype.

In this study, we used the genomics profiles to examine non-genetic mechanisms underlying drug tolerance. Cells capable of counteracting excessive replication stress and p53-driven

apoptosis could be present or acquire tolerance via rewiring of their intrinsic TF-network. Gene regulatory networks are known to embed multiple mutually exclusive TF activity configurations that can encode switch-like cellular decisions (Wray, Deltcheva et al. 2022). Our results indicate that WEE1 inhibition critically impacted the ability of KMT2A-r cells to sustain the RUNX1-GATA2-MYC driven regulatory program. Upon disruption of this progenitor program, alternative TFs could reroute cell fate decision favoring survival in absence of RUNX1-MYC. Notably, we found increased chromatin access at several TF motifs typically activated at later differentiation stages (Mehtonen et al 2020) and correspondingly the expression and accessibility of genes encoding the pro-survival BCR- and PI3K signaling components, including co-expression of BCL6 and pre-BCR signaling. Although KMT2A-r leukemias resemble the early lymphoid/multipotent progenitors by immunophenotype, recent single cell characterization of patient cells has revealed that the transcriptional programs of a subset of cells present in primary bone marrow tissue match more mature, pro- and pre-B-like differentiation states (Chen, Yu et al. 2022)(Khabirova, Jardine et al. 2022). Similarly, our previous single cell genomics study deciphering features of drug resistance directly in ALL patients during induction chemotherapy (Mehtonen, Teppo et al. 2020) demonstrated that although the diagnostic blasts (ETV6-RUNX1 subtype) matched pro-B-like cell state, the persisting leukemic cells at day 15 are re-programmed towards pre-B TF activity state, highlighting the clinical relevance of a non-genetic route to drug tolerant state.

The TF activity changes that characterized the more drug-tolerant cell state III included increased NfKB TF motif access at chromatin and elevated BCL6 expression, both corresponding to TFs known to counteract p53-driven apoptosis and repress genes involved in sensing or responding to DNA damage (Webster and Perkins 1999) (Ranuncolo, Polo et al. 2008) (Phan and Dalla-Favera 2004). BCL6 and pre-BCR- signaling can form an oncogenic feedback loop in ALL cells that promotes survival signaling via SRC family kinases, SYK,

ZAP70, and downstream PI3K activation (Geng, Hurtz et al. 2015). Due to the recent development of efficient drugs inhibiting these pathways (dasatinib, ibrutinib), this resistance could potentially be disrupted. High BCL6 at diagnosis was proposed as a prognostic biomarker (Hurtz, Chan et al. 2019). However, we show that upon genotoxic stress, cells could rapidly switch to BCL6+ state, indicating that BCL6 might prime cells for the emergence of acquired resistance during continuous treatments, and thus represent a dynamic biomarker that could be monitored at early treatment time points. Our results further implicate regulation of lipid metabolism (LXR, SREBF) as a concomitant change that has been recognized in immune cell activation and oncogenic PI3K signaling in different cancers (Bensinger, Bradley et al. 2008, Ricoult, Yecies et al. 2016). MEF2D-fusions that define a rare ALL subtype with unfavorable prognosis harbor constitutive activity of a TF circuit including BCL6 and SREBF1 (Tsuzuki, Yasuda et al. 2020). Here, we compared the *in vivo* drug response in a primary KMT2A-r xenograft and a MEF2D-fusion patient sample. The highly correlated gene expression of the respective TFs and their target genes gives prominence to the relevance of this pro-survival circuit as a tolerance mechanism upon cell cycle targeting (AZD1775, or vincristine, respectively). These findings provided the rationale for strategies to target the ALL cells that acquire this phenotype and persisted upon AZD1775 treatment. By interfering with pro-survival signaling through targeting lipid metabolism or inhibition of BCR signaling, sequential administration of mTOR inhibitor AZD2014, fatostatin and even more potently inhibitors of BCR-signaling (dasatinib, ibrutinib), completely blocked recovery of KMT2A-r *in vitro*. Notably, this strategy strongly reduced recovery also in Nalm-6 cells, indicating that sequential targeting of WEE1 and BCR or metabolic activity, may be effective more broadly in pre-BCR+ ALLs.

Our results, consistent with a number of ALL drug therapy studies, indicate that targeting specific cancer vulnerabilities using carefully designed drug scheduling, may represent the most

useful measures for improving leukemia treatment success and counteracting disease recurrence. Despite existing data of potent chemo-sensitizing activities of AZD1775 in combination with different cytotoxic agents (Tibes, Bogenberger et al. 2012, Van Linden, Baturin et al. 2013, Ford, Baturin et al. 2015, Garcia, Snedeker et al. 2017), WEE1 inhibitors have not been tested, to our knowledge, in ALL clinical trials. To date, several ongoing efforts aim to introduce immunotherapy in B-ALL treatment which requires implementation of a successful chemotherapy regime to initially reduce the leukemia burden, followed by immunotherapy. Combination therapies with WEE1 inhibitors may be attractive in this setting, reducing leukemia burden by inducing cell death through the cell-intrinsic mechanism, as characterized here. In solid cancers, favorable responses have been reported in phase 3 trials, though concerns in toxicity remain when combined to strongly cytotoxic backbone drug therapies. Our results show that several low toxicity drugs, already in clinical use for ALL or other non-communicable disease, potentiate the efficacy of AZD1775 in leukemia to overcome this challenge. Furthermore, AZD1775 was recently reported to additionally activate immune signaling through activation of STING and STAT1 pathways, or the double-stranded RNA viral defense pathway, and sensitize solid tumors to immune checkpoint therapy (Guo, Xiao et al. 2022), (Taniguchi, Caeser et al. 2022). Pre-clinical testing in xenograft models lacking the immune system, as used here, may therefore only partially represent the efficacy of AZD1775 monotherapy. In this study, we demonstrated that drug scheduling has a critical impact on treatment efficacy. Concurrent drug combinations with WEE1 inhibition were unable to counteract cell recovery. This result supports a model where the drug-induced persister cell state can be eradicated only succeeding activation of the cell-intrinsic signaling pathways founding a drug-tolerant cell state. Relating drug responses to functional cell fate mapping will therefore be critical in the future, and precision treatment could be implemented as first line

therapy based on anticipated adaptive cellular response dynamics (Sicklick, Kato et al. 2021, Alkhatib, Rubinstein et al. 2022).

In summary, the combination of biochemical assays and cellular resolution genomics analyses provided new insight on pronounced remodelling of the gene regulatory landscape upon cell cycle checkpoint targeting. Based on the results, we propose a strategy for WEE1 inhibition in ALL that anticipates the TF network re-wiring and switch to a pre-BCR+BCL6+ cell state and targets the drug-tolerant phenotypes identified in this study through novel sequential drug administration, establishing a proof-of-concept that could be utilized in the design of new targeted drug screens and clinical trials.

COMPETING INTERESTS

The authors declare no competing interests.

ACKNOWLEDGEMENTS

The authors thank Professor Richard Lock (Children's Cancer Institute Australia) for providing PDX samples and related clinical information for this study. This research was funded by The Swedish Childhood Cancer Fund, the Swedish Cancer Society, The Swedish Research Council, Karolinska Institute, Radiumhemmets Research Foundation, AstraZeneca-SLL-KI Open Innovation grant (#18122013), the Academy of Finland (321553, 310106), ERA-NET ERA PerMed, Väre Foundation, Emil Aaltonen Foundation, Cancer Foundation Finland, Jane and Aatos Erkko foundation, and Sigrid Juselius foundation. The authors wish to acknowledge CSC – IT Center for Science, Finland and UEF Bioinformatics Center, University of Eastern Finland, Finland for computational resources. The authors would like to Acknowledge Clinical

Genomics Lund, SciLifeLab and Center for Translational Genomics (CTG), Lund University, for providing expertise and service with sequencing and analysis.

METHODS

Cell culture

A panel of ALL cell lines consisting of T-ALL: T-ALL1, Peer, Molt-16 and B-ALL cell lines: Nalm-6 (ETV6-PDGFRB); 697, RCH-ACV, Kasumi-2, MHH-Call3 (TCF3-PBX1); REH (ETV6/RUNX1); RS4;11, SEM, ALL-PO, KOPN8 (MLLr-ALL); SupB15, TMD5 (BCR-ABL) were purchased from the The Department of Human and Animal Cell Lines (DSMZ). Cell lines were maintained in RPMI1640 (Gibco, Thermo Fisher) supplemented with 10% FBS (Gibco, Thermo Fisher) and 2 mM L-glutamine (Gibco, Thermo Fisher) and 10 mM HEPES (Gibco, Thermo Fisher).

Drug and dose response assessment

AZD1775, AZD2014 (Astra Zeneca), Dasatinib, Ibrutinib and Fatostatin (MedChemExpress, Europe), were reconstituted in dimethyl sulfoxide. Drugs were stored in aliquots at −20 °C. Alamar Blue assay was used to determine cell viability of the cells treated with increasing doses of drugs for 72 hours. Cells (30000 cells/well) were seeded into 96-well plates. Following drug treatment as indicated for 72 h, cell viability was measured using a Alamar Blue assay according to the manufacturer protocol. For the recovery of proliferation cells were treated for 72 or 96 hours and allowed to recover for an additional 10-14 days without the drugs. Regrowth was assessed by Alamar Blue staining. Absorbance was measured at 760 nm by spectrophotometer. All experiments were repeated three times.

Analysis of apoptosis using fluorescence live cell microscopy Cells were stained with Incucyte® Caspase-3/7 Dye for Apoptosis (Sartorius) according to the manufacturer's

instructions, followed by live cell microscopy performed with an IncuCyte S3 Live Cell Analysis System (Essen Bioscience). Nine planes of view were collected per well, using the 20x objective. The obtained data were analyzed with the IncuCyte S3 Cell-by-Cell Analysis Software Module (Essen Bioscience).

Western blotting

For biochemical analyses of protein phosphorylation and total level, the cells were lysed in NP-40 lysis buffer (50 mM Tris-HCl pH 8.0, 150 mM NaCl, 1% NP-40) supplemented with both protease (Complete mini, Roche) and phosphatase (PhosSTOP, Roche) inhibitors. Proteins were resolved in -12% Bisacrylamide gel under reducing-denaturing condition, blotted on to PVDF membrane, and detected by immunoblotting using the appropriate antibodies. The list of antibodies and their sources can be found in the appendix file.

Analysis of bulk gene expression data in HEMAP. Normalized and log-transformed gene expression levels were compared between different hematologic malignancies or ALL subtypes based on the Wilcox test (Polonen, Mehtonen et al. 2019).

PDX transplantation and AZD1775 treatment

In-house bred NOD.Cg-*Prkdc*^{scid} *Il2rg*^{tm1Wjl}/SzJ (NSG) mice of 8-9 weeks were sublethally irradiated (250cGy) and 24 hours later, mice were transplanted through the tail vein with $2{\cdot}10^6$ cells from the MLL-7 donor, established from a diagnostic sample from a child with ALL and the *KMT2A::AFF1* fusion gene (courtesy of Dr. Richard Lock) (Lock, Liem et al. 2002) Ciprofloxacin (KRKA, Stockholm, Sweden) was given in the drinking water for the duration of the experiment. A 1% engraftment of hCD45$^+$hCD19$^+$ cells was set as a starting point for the treatment. Engraftment was checked by taking 60 µl of blood from *vena saphena* 14 days after transplantation and then engraftment was reassessed every other day if the 1% hCD45$^+$hCD19$^+$

was not reached. Red blood cells were lysed with ammonium chloride (Stemcell technologies, Cambridge, United Kingdom), washed in PBS (GE Healthcare Life Sciences, Logan, UT, USA) + 2% FBS (Thermo Scientific, Waltham, MA, USA), blocked with 10% mouse serum (#M5905, Sigma Aldrich) and stained with the following antibodies: anti-human CD45-APC (clone HI30, #555485, BD Bioscience, Franklin Lakes, NJ, USA) (hCD45) and anti-human CD19-APC/Cy7 (clone HIB19, #302217, Biolegend, San Diego, CA, USA) (hCD19). Dead cells were excluded with Draq7 (Biolegend). Flow cytometric analysis was performed using the LSRFortessa (BD Biosciences) and data analysis using the FlowJo software (FlowJo, LLC, Ashland, OR, USA). Once the desired engraftment of 1% of human cells was achieved, mice (N=3 per group) were either treated with 120 mg/kg of AZD1775 (#HY-10993 MedChemExpress, Monmouth Junction, NJ, USA) 5 days a week, for 21 days (5 days on, 2 days off) (Figure S1D-H) for the survival experiment, or 48 hours with 120 mg/kg AZD1775 (#HY-10993) every 24h, and 4 hours after the last dose. Before the mice were sacrificed , blood was taken from *vena saphena*, and mice were then euthanized by cervical dislocation. Upon sacrifice, an autopsy was performed and bone marrow cells from the tibia, femur, and hip from both legs, as well as from the spleen, were collected and homogenized into single-cell suspensions by manual trituration and viably frozen in 10% DMSO (Sigma-Aldrich, Saint Louis, Missouri, USA) in FBS (Thermo Scientific). Mice were bred and maintained in accordance with Lund University's ethical regulations and approved by the local ethics committee of Lund, Sweden.

GRO-seq assay. To analyze the actively transcribing RNA polymerases genome-wide, GRO-seq assays were performed as in (Heinaniemi, Vuorenmaa et al. 2016). Five million nuclei were collected from RS4;11 cells after 4, 10 and 24 h AZD1775 or DMSO treatment. The nuclear run-on reaction buffer (496 mM KCl, 16.5 mM Tris-HCl, 8.25 mM MgCl2 and

1.65% Sarkosyl (Sigma-Aldrich, Steinheim, Germany) was supplemented with 1.5 mM DTT, 750 µM ATP, 750 µM GTP, 4.5 µM CTP, 750 µM Br-UTP (Santa Cruz sc-214314A, Biotechnology, Inc., Dallas, Texas, USA and Sigma-Aldrich B7166) and RNAse inhibitors (RNase Inhibitor (Thermo Fisher, Carlsbad, CA, USA, and RNasin® Plus RNase Inhibitor Promega). To each 100 µl of nuclei samples 50 µl of the run-on reaction buffer was added and incubated for 5 min at 30°C. The RNA was collected using Trizol LS, fragmented and run-on reaction products were immuno-purified two times using anti-Br-UTP antibody (ab-6326, Abcam) bound to 30 µl of magnetic beads (Protein G DynabeadsThermo Fisher Scientific) and washed with 300 µl of PBST wash buffer four times (refer to detailed protocol in Roberts et al. 2015). The cDNA template was PCR amplified (Illumina barcoding) for 12 cycles and size selected to 225–350 bp length. The ready libraries were sequenced with Illumina Hi-Seq2000 (GeneCore, EMBL Heidelberg, Germany).

ChIP-seq. To distinguish the signal corresponding to active enhancer regions from the collected GRO-seq profiles, RS4;11 cells were similarly treated for 4, 10 and 24 h with AZD1775 or DMSO and cells were crosslinked with 1/10 of volume of 11% formaldehyde solution (37% formaldehyde (Sigma-Aldrich), 5M NaCl, 0.5 M EDTA pH 8.0, 0.5M EGTA, 1M HEPES) for 10 mins gently rotating at 2 mio/ml cell concentration in media. The reactions were quenched by adding glycine to a final concentration of 120 mM, and cells were washed twice with ice-cold PBS. Crosslinked lysate was flash frozen with liquid nitrogen and stored at - 80°C. Lysates were thawed, nuclei were extracted, and MNase treated and antibody bound chromatin collected by adding 25 µl of Dynabeads Protein G (Thermo Fisher Scientific) and rotating for 1 hour at 4°C as previously described (Heinäniemi, Vuorenmaa et al. 2016) with the following minor modifications: 5 U- 1U of MNase (Thermo Fisher Scientific) was used and 5 cycles sonicated then (Bioruptor® Plus and Bioruptor® Next Gen, Diagenode). Then

supernatant was diluted to dilution buffer 2.5 times. Samples were pre-cleared with Protein G Dynabeads (Thermo Fisher Scientific) using 25µl per sample (1 h 4°C rotating). Subsequently, input samples were taken. 2.5 µg of specific H3K27ac antibody (cat# ab4729, Abcam) for 5-9 million cells were used. Beads were washed with 1 ml of cold wash buffers wash buffers I, II and III as in for 3 minutes (Heinäniemi, Vuorenmaa et al. 2016). Finally, beads were washed twice with TE-buffer. Beads were eluted twice in elution buffer (1% SDS, 100mM NaHCO3). Immunoprecipitated chromatin was reversecrosslinked by adding NaCl for a final concentration of 0.2M and 0,4mg/ml of RNAse A (Invitrogen) was added to each sample for 16h at 65°C. Proteinase K treated by adding 31µl of Proteinase K buffer (161mM EDTA, 645mM Tris pH7.4, Proteinase K 0,65mg/ml (Thermo Fisher Scientific)) for 1 h at 50°C. For DNA purification, ChIP DNA Clean & Concentrator (ZymoResearch, Irvine, CA, USA) was used like manufacture´s protocol. ChIP-Seq libraries were prepared as previously described (Heinäniemi, Vuorenmaa et al. 2016) (Heinz, Benner et al. 2010) with samples PCR amplified for 13-14 cycles and size selected for 225-350 bp fragments by gel extraction. Single-end sequencing (75 bp) was performed with Illumina NextSeq 500/550 High Output Kit v2.5.

GRO-seq read processing GRO-Seq reads were quality controlled (FastQC). Reads were adapter trimmed using HOMER (version 4.9 (Heinz, Benner et al. 2010) and filtered (min 95% of positions have a min phred quality score of 10) using the FastX toolkit (http://hannonlab.cshl.edu/fastx_toolkit/). Reads mapping to rRNA regions (AbundantSequences as annotated by iGenomes) were discarded. The Bowtie software (version 1.1.2 Langmead et al., 2009) was then used for alignment of remaining reads to the hg19 genome version, allowing up to two mismatches and no more than three matching locations. The best alignment was reported. Reads corresponding with so-called blacklisted regions that include unusual low or high mappability as defined by ENCODE, ribosomal and

small nucleolar RNA (snoRNA) loci from ENCODE and a custom collection of unusually high signal depth regions from GRO-seq was used to filter the data. GRO-seq tagDirectories were generated from aligned reads with fragment length set to 75 and data visualized using makeMultiWigHub.pl with strand-specificity HOMER (version 4.9).

ChIP-seq read processing Reads with poor quality bases scores were filtered (min 97% of positions were required to have a min phred quality score of 10) using the FastX toolkit (http://hannonlab.cshl.edu/fastx_toolkit/). Duplicate reads were collapsed using fastx (collapse). Bowtie (version 1.2.3 (Langmead, Schatz et al. 2009) was used to align the reads to the hg19 genome version, allowing up to two mismatches and no more than three matching locations. tagDirectories were generated with HOMER (version 4.9) tool. Histone peaks (GSE148195) were identified using HOMER (version 4.9) findPeaks with setting -style histone. The peak signal profile across pooled tagdirs was then used to distinguish dips that correspond to nucleosome free regions that can be accessed by TFs (this was found to work well for peaks < 7.5 kb).

GRO-seq gene signal analysis To compare the effect of AZD1775 on primary transcript levels across the collected time points Refseq (genome_annot_hg19 refGene_2018) coding and non-coding gene coordinates were quantified without exon regions. A raw count matrix was generated using Homer (version 4.9.1) specifying as maximum read per position 3. not allowing combining quantified reads if the same transcripts is detected more than one time. The low expression transcripts were filtered based on cpm and rpkm values requiring a row sum greater than 0.5 in at least two samples. To detect differentially expressed transcripts, a generalize linear model was fit using functions available in the R/Bioconductor package edgeR. Genes with significant change between any of the conditions (adjusted p-value < 0.001) were reported

based on one-way ANOVA-like the likelihood ratio tested with glmLRT function. The genes were then clustered using k-means (into six clusters) and plotted as a heatmap (ComplexHeatmap R package) with six clusters. One cluster profile was excluded as it reflected mainly changes in DMSO basal levels between time points. Pathway analysis was performed on the gene clusters with > 100 genes, otherwise the genes were plotted and examined individually.

GRO-seq enhancer signal analysis The nascent transcriptome result allows quantification of eRNA signal that can guide the analysis of TF activity. Enhancer regions are typically defined based on multiple genomic signal features. Here we started with DNA hypersensitive sites (DHS from Encode Duke narrow peaks, available across the ENCODE cell collection) and ATAC-seq peak coordinates (from RS4;11 cells in GSE117865 and from bone marrow cell populations in Ulirsch et al 2019) for specifying candidate enhancer centers. The candidate regions were extended +/- 500 bp and the 1 kb size enhancer regions were quantified with Homer (homer/4.9.1) analyzeRNA. Coordinates with overlap with gene sense-transcription or the promoter region signal were excluded. Enhancers that passed a minimum cpm cutoff or intersected (bedtools2/2.27.1) with RS4;11 histone ChIP-seq peaks for H3K4me1 (GSE71616) and H3K27ac (our own GSE148195, GSE71616 and GSE117865) were kept for analysis. Intergenic enhancers should have bidirectional and approximately equal signal from plus and minus strand. If the mean difference was over 10-fold only the lower signal was considered (the stronger signal typically derives from transcribed gene region signal extending beyond annotated transcription termination site). For tightly clustered enhancers, the enhancer that overlapped best with RS4;11 ATAC or centered nuclear free region (< 7.5kb peak size) of H3K27ac peaks was selected, or otherwise the region with maximum signal was used. Quantified enhancers were filtered (expression cut-off 5 in minimum two samples) and

normalization using RLE. A quasi-likelihood negative binomial generalized log-linear model was fitted using edgeR. The quasi-likelihood (QL) F-test was used to detect significant eRNA level changes (FDR < 0.1) Clustering was performed using hierarchical clustering and distinct cluster profiles were visualized using the R package ComplexHeatmap. Denovo motif discovery was performed by extracting the DNA sequence for motif enrichment analysis with Homer (4.9.1) findMotifsGenome.pl (region size 200bp, repeat masked genome, background all enhancers from statistical analysis. To further visualize enhancer signal GRO-seq signal histograms were generated. For TF binding sites, intergenic region corresponding to motif-centered TF ChIP-seq peaks were used for signal summary. p53 ChIP peaks were retrieved from GSE46991 and centered with TP53 motif (p63(p53)/Keratinocyte-p63-ChIP-Seq(GSE17611)/Homer) The histogram was generated with bin size 25 bp +/-2000bp from the ChIP-peak center. For chromatin state-specific enhancer analysis regions that had high/low accessibility in each chromatin state were detected using the Seurat Findmarkers function, with a minimum fold change difference of 0.1 and adjusted p-value a 0.1 To further visualize top 200 chromatin state specific enhancer signals the assay-specific signal matrixes were generated with annotatePeaks.pl tool of the HOMER package (version 4.11 (Heinz, Benner et al. 2010). The matrixes were generated with bin size 25 bp +/-1000 bp from the enhancer center. Visualization was done with image J (version 1.53t (Schneider, Rasband et al. 2012) and average signal summary histograms generated with the same parameters visualized with base R plots (R version 4.1.0).

scRNA-seq assay. To analyze the drug response at cellular resolution RS4;11 or Nalm-6 cells were treated for 24 h with 1 µM AZD1775 or DMSO. Cell viability was checked using Trypan blue with Cellometer Mini Automated Cell Counter (Nexcelom Bioscience) and only viable cells were processed further. To deplete dead cells, the Dead Cell Removal Kit (#130-090-101,

MACS miltenyi Biotech) was used and the column rinsed twice with 1 ml Binding Buffer to elute viable cells (97-98% viability). Single cell suspension, loading and library preparation was performed according to the ChromiumTM Chromium Single Cell 3´Reagent Kits v3 User guide CG000184 Rev A and libraries constructed using the 10X Genomics Chromium technology. Loading concentrations were 1700 cell/ul, 1000cell/ul for RS4;11 DMSO, AZD1775 cells; 500 cell/ul, 1300 cell/ul Nalm-6 DMSO, AZD1775, respectively. Each lane was loaded with 10 000 cells as pools of human and mouse cells (not part of this study) processed in parallel. Sequencing was performed in FIMM Technology Center Sequencing Laboratory, Biomedicum, Helsinki, Finland by using a NovaSeq S2 sequencer aiming 50 000 reads per cell depth.

PDX cell staining and sorting for scRNA-sequencing

Sample preparation for scRNA-sequencing was performed by thawing viably frozen bone marrow cells, which were stained with Draq7 (BioLegend), hCD45 (BD Bioscience), and hCD19 (BioLegend), together with a PerCP/Cyanine5.5 anti-mouse CD45 (BioLegend). Approximately 20.000 alive/mCD45^{-}/hCD45^{+}/hCD19^{+} cells were sorted into a PBS (GE Healthcare Life Sciences) + 2% FBS (Thermo Scientific) coated tube and prepared for sequencing using the 10x Genomics platform at the Center for Translational Genomics, Lund University.

scMultiome-seq assay To analyze the drug response transcriptional and chromatin accessibility from the same cells, RS4;11 were treated for 10 h with 1 µM AZD1775 or DMSO. In scMultiome assay nuclei were first isolated. 10x Genomics protocol (User guide CG000365 RevB) was first optimized for the RS4;11 cell line with a 3-minute cell lysis time. Nuclei were then washed 3 times with 600 g 7 min centrifugations steps. Nuclei quality was determined

with light microscoping at 40x focus. Nuclei count and lysis optimalization was determined with diluted Trypan blue solution with Countess 3 cell counter (Invitrogen). Each sample was loaded with 10 000 nuclei and library preparation performed according to the Chromium Next GEM Single Cell Multiome ATAC + Gene Expression User guide CG000338 Rev E and libraries constructed using the 10X Genomics Chromium technology. Loading concentrations were 7200 nuclei/ul for DMSO cells and 4860 nuclei/ul for AZD1775 cells. Multiome ATAC Sequencing was performed in Novogene Cambridge, United Kingdom by using a NovaSeq PE50 sequencer aiming 20 000 reads per cell depth. Multiome RNA samples were sequenced in the same place with NovaSeq PE150 aiming 50 000 reads per cell depth.

scRNA-seq read processing scRNA-seq data was processed and aligned with Cell Ranger (version 3.0.2) using hg19 and mm10 genome as reference. Only the human cell counts were used for future analysis performed using the R package Seurat (v3) and the Python package Scanpy (version 1.5.1). Data per cell line was filtered with the following cutoffs: cells had more than 2000 and less than 6000 UMIs, percentage of mitochondrial counts less than 20%, and less than 500 mouse mm10 gene counts. Post-filtering, RS4;11 DMSO had 4169 cells and AZD1775 sample respectively 5135 cells. Post-filtering, Nalm-6 DMSO had 5598 cells and Nalm-6 AZD1775 sample resulted in 5039 cells. Cells were log-normalized using scaling factor of 10 000.

PDX cell scRNA-seq data was processed and aligned with Cell Ranger (version 6.0.1) using GRCh38-2020-A genome as reference. Utilization of R package Seurat (v3) enabled further analysis. MLL-7 data was filtered with the following cutoffs: cells had more than 1500 but less than 6000 UMIs and percentage of mitochondrial counts less than 10%. Post-filtering, DMSO had 4432 cells and AZD1775 resulted in 4672 cells. Cells were log-normalized using a scaling

factor of 10 000. Vst selection method (Seurat) was implemented to select 2000 highly variable features (genes). DMSO and AZD1775 cells were clustered using the FindNeighbors function based on PCA dimension 1:10 and with resolution 0.5. This resulted in a discovery of 7 distinct cell clusters in DMSO and treated cells.

scRNA-seq cell state analysis Vst selection method (Seurat) was used to select 2000 highly variable features (genes). Cells were clustered using the FindNeighbors function based on PCA dimension 1:10 and with resolution 0.5. This resulted in a discovery of 11 distinct cell clusters in RS4;11 cells that are referred to as “cell states”. UMAP visualizations were used to represent the data in two dimensions. For cell cycle characterization, a list of cell cycle markers from Tirosh et al. 2015 were utilized. Several statistical comparisons between the cells assigned to these cell states were performed: i) Genes that had high/low expression in each cluster were detected using the Seurat Findmarkers function, with a minimum fold change difference of 0.25 and adjusted p-value between cells assigned to the cluster and other cells. ii) AZD1775-treatment specific cell states were compared with the cell state matched to normal cell cycle G2/M-phase (cell state 4), iii) cluster markers were detected between AZD1775-treatment specific cell states. Violin plots were used to visualize gene expression distributions. For visualizing gene expression level per cell state all unique genes from cluster comparisons were acquired and the mean scaled counts were summarized by cell type. These mean expression values were then used as input for hierarchical clustering with 1-pearson correlation as a distance metric. ComlexHeatmap R package was used for visualizations, testing different cluster numbers (10-20) for row-wise clustering. Pathway analysis was performed for the gene clusters and for broader patterns distinguished based on the heatmap.

scMultiome-seq read processing

For comparing to 24 h data, multiome scRNA-seq data was processed with the same Cellranger preprocessing workflow, resulting in reads mapped to hg19 genome version. DMSO and AZD1775 samples were merged and analyzed using Seurat v4.1.1 using the following cutoffs in filtering: 1500 < UMIs < 6000 UMIs and percentage of mitochondrial counts < 20%, resulting in 12835 DMSO and 14788 AZD1775 cells. The raw reads were also processed and aligned with Cell Ranger Multiome workflow (cellranger-arc-2.0.1, hg38 genome version). The cell assignment available from per barcode metrics output was used to select nuclei for downstream analyses. The scATAC-seq workflow based on Signac ((Stuart, Butler et al. 2019) 0.1.6 and Seurat 3.1.1. versions that was used for 24 h data was run with minor modifications (EnsDb.Hsapiens.v86, no blacklist filtering, atac_peak_region_fragments > 1000 & atac_peak_region_fragments < 100000 & pct_reads_in_peaks > 50 & nucleosome_signal < 10) to generate comparable results. Nucleosome signal histogram analyses were performed using Signac version 1.6.0. The matching cell barcodes between scRNA- and scATAC-seq profiles from the same cells were utilized to visualize data across modalities. For example, this allowed showing the scATAC-seq nucleosome signal on the UMAP generated from scRNA-seq data. Cell type labels were assigned based on label transfer analysis with the respective 24 h sample used as reference sample.

scRNA-seq RNA velocity and PAGA analysis

Dynamic changes in gene transcription can be modelled based on reads corresponding to both unspliced and splices mRNA (newly synthetized RNA vs processed RNA, respectively). Based on the dynamic RNA processing model (La Manno, Soldatov et al. 2018), the future transcriptome state can be visualized together with the measured current state. This analysis was used to analyze cell state dynamics in the RS4;11 cell model. Velocyto CLI (version 0.17.17 (La Manno, Soldatov et al. 2018)) was used to calculate the count matrices, masking

expressed repetitive elements (available for hg19 from UCSC Genome Browser). The scVelo-package (version 0.2.1 (Bergen, Lange et al. 2020)) was used in downstream analysis. The gene expression matrix was accompanied with the spliced and unspliced count matrices. The data was first filtered by removing genes with less than 20 shared counts in both spliced and unspliced data. The matrices were each then normalized by dividing the counts in each cell with the median of total counts per cell. The 2000 most variable genes were extracted based on the spliced count matrix and the data matrices were log-transformed. Top PCs (30) were used for neighborhood graph calculation, with the number of neighbors set to 30. Then the AZD1775 and DMSO samples were separated for RNA velocity analysis. Based on the neighborhood connectivities, the first order moments for spliced and unspliced matrices were calculated and the velocity estimated using the dynamical model. The velocities were embedded to a UMAP presentation, which was calculated with 20 PCs and 10 neighbors. A PAGA graph was used to visualize connectivities (dashed lines) and transitions (solid lines). Python Scanpy-package (version 1.5.1) was used for gene set scoring. Before scoring, gene sets used in the analysis (e.g. senescence gene sets) were filtered to include only genes that are expressed in the data, excluding G2M-phase markers (to remove cell cycle bias in the scores).

scATAC-seq assay. RS4;11 cell nuclei were collected from parallel cell cultures as those used for the scRNAseq experiments to study chromatin accessibility at the single cell level (scATAC-seq). Nuclei were isolated with 10x Genomics Nuclei Isolation for Single Cell ATAC Sequencing user guide CG000169 Rev D. Nuclei quality was determined with light microscoping with a 40x focus. Nuclei concentration was determined with Trypan blue and pools of human and mouse (not part of this study) cell lines were loaded together. scATAC-seq was performed using Chromium Single Cell ATAC Library & Gel Bead and Chip E Single Cell ATAC Kit (10x Genomics), user guide CG000168 Rev C. Sequencing was performed in the

FIMM Technology Center Sequencing Laboratory, Biomedicum, Helsinki, Finland using NovaSeq S2 sequencer aiming 50 000 reads per cell depth.

scATAC-seq read processing

The raw reads were processed and aligned with Cell Ranger atac workflow (version 1.2.0). Seurat ((Stuart, Butler et al. 2019), version 3.1.1) package and Signac ((Stuart, Butler et al. 2019), version 0.1.6) were used for downstream analysis, selecting only the human peak coordinates and cells. Peaks detected from DMSO and AZD1775 treated cells were merged using bedtools (version 2.27.1), discarding < 10 bp wide peaks. Data across treatments was combined by re-quantifying counts from the fragment files based on the merged peak regions. Peaks detected in > 1% of cells were kept for downstream analyses. Nucleosome signal was quantified based on fragments mapping to chr 1 using the Signac package NucleosomeSignal function. TSS enrichment was calculated based on coordinate ranges retrieved from EnsDb.Hsapiens.v75. These quality metrics were used in combination with metrics to select good quality nuclei for downstream analyses (peak region fragments > 1000, peak region fragments < 100000, percentage reads in peaks > 15, blacklist ratio < 0.05, nucleosome signal < 10, TSS.enrichment > 2). To analyze the atypical nucleosome signal manifest in AZD1775-treated sample, the above filtering criteria were used without the nucleosome signal cutoff to plot the signal profiles. Term frequency-inverse document frequency (TF-IDF) normalization of peaks by accessibility was performed using the LSI implementation used by (Cusanovich, Hill et al. 2018). To reduce dimensions and perform clustering of the data matrix, singular value decomposition (SVD) was run on the TD-IDF normalized matrix, keeping 150 dimensions. Based on elbow plot analysis 50 dimensions were kept for UMAP visualization and clustering. To study more specifically chromatin activity responses at each treatment condition, separate UMAPs were created (reduction method lsi, dims=1:50, resolution 0.4). The two smallest

chromatin states found in the chromatin state clustering of DMSO (c5, c6) and AZD1775 (c6, c7) treated cells differed based on quality control metrics. The smallest clusters had a low peak region fragment amount (low quality) and were discarded from downstream analyses. The clusters with elevated nucleosomal signal were reproduced in the scMultiome result and could be matched using this data to cells with a good quality RNA-seq profile. Moreover, they had a distinct TF motif activity pattern in ChromVar analysis (unlike the smallest cluster). Therefore, we kept the clusters with elevated nucleosome signal in the downstream analyses.

TF motif activity profile from scATAC-seq profile

To determine motif activity, i.e. variability in chromatin accessibility per cell, the chromVAR ((Schep, Wu et al. 2017), version 1.6.0) tool was applied separately to each sample. The known TF motifs available in the Homer tool were scored. Subsequently, cluster specific motifs were detected using statistical analysis (Seurat FindMarkers function, log2 fold change threshold 1.5, adjusted p-value <0.0001) comparing each chromatin cluster to other clusters. Redundant motifs recognized by similar protein complexes were grouped manually and the most significant motif kept for visualization. The scaled chromatin accessibility values were used to calculate mean access per chromatin cluster and visualized using the ComplexHeatmap R package. The Signac visualization functions were used to generate genome browser track plots comparing different clusters.

Label transfer from scRNA-seq to scMultiome-seq

To characterize similar cells between transcriptome level in two different time points the canonical correlation analysis available in the Seurat (Seurat 4.1.1) package was used. First anchors between two different time points were identified following the user guide recommendations. 24 h RS4;11 data cell states 1-11 were used as reference. Then the 24 h

RS4;11 cell state labels were transferred to the 10 h multiome scRNA-seq data. Prediction scores were visualized for quality control purposes (refer to Fig. S2) and all predicted cells were applied in further analysis. The same analysis was performed to characterize two different time point chromatin levels with user guide recommendation for ATAC data. 24 h RS4;11 DMSO ATAC clusters 0- 5 were used as reference for 10 h DMSO multiome scATAC-seq data. 24 h RS4;11 AZD1775 ATAC clusters 0- 6 were used as reference for 10 h AZD1775 multiome scATAC-seq data. Prediction scores were visualized for quality control purposes (refer to Fig. S2G) and a prediction score < 0.3 omitted cells with a poor match from visualizations (assigned to category NA).

Pathway enrichment analysis

Gene lists acquired bulk genome wide and scRNA-seq studies were analyzed using the online web server Enrichr (Chen, Tan et al. 2013, Kuleshov, Jones et al. 2016) for enrichment of ontology and pathway terms. The analysis was performed based on gene sets from BioPlanet 2019 and TF perturbations. Enriched terms were ranked based on lowest adjusted p-value and top terms per group visualized as dot plots (R package ggplot2).

Cell proliferation, EdU incorporation and senescence assessment by FACS

To study the effects of AZD1775 on cell proliferation, cells were incubated with 10 μM EdU for 1 hour at 37 ◦C to label proliferating cell population. EdU-labelling of the cells were done prior the treatment for further processing according to the kit protocol (Thermo Fisher). Following cell fixation and permeabilization, the cells were stained with pH3 (1:25, BD Bioscience), and 50 μg / mL Propidium Iodide in 1% BSA/ TBS – 0.5% Tween 20 containing 10 μg/mL RNAseA overnight at 4 ◦C. Finally, the click- iT reaction were carried out according to the manufacturer's protocol prior to FACS analysis. To analyze senescence, treated cells

were or CellEvent Senescence Green Flow Cytometry Assay Kit (Invitrogen, C10840) and Propidium Iodide according manufacturer's protocol.

Quantitative real-time PCR (qRT-PCR)

To perform the qRT-PCR, RNA was prepared using RNeasy kit (Qiagen). Residual genomic DNA was eliminated from the total RNA fraction by DNase I treatment (Qiagen), according to the manufacturer's protocol (Qiagen). 50 ng of the purified RNA was then used for cDNA synthesis (SuperScript VILO cDNA Synthesis Kit, Invitrogen, Life Technologies). Quantitative PCR were carried out using SYBR green probes as described in the appendix file (Table S5). The data were analyzed with ΔΔCt method and presented as relative expression.

Statistical analysis

Data from biochemical assays are presented as the mean + SD from two or more independent experiments unless indicated otherwise. Statistical analyses were performed using the statistical package GraphPad Prism 8 (GraphPad Software, San Diego, CA, U.S.A. http://www.graphpad.com) using either Student's t-test, Log-rank (Mantel-Cox), one-way analysis of variance (ANOVA) or two-way analysis of variance (ANOVA), as indicated. Genome-wide statistical analysis was performed using dedicated software (R or Python packages as indicated). Multiple testing correction was performed using Benjamini-Hochberg or Bonferroni's post hoc test when appropriate.

Availability of data and materials

The single cell datasets analyzed and generated in the current study will be available in Gene Expression Omnibus under the accession number when manuscript will be published. Bulk data for GRO-seq in the RS4;11 cell line will be available in GEO after published. Additional data for ChIP-seq peak analysis was downloaded from GEO GSE71616 https://www.ncbi.nlm.nih.gov/geo/query/acc.cgi?acc=GSE71616, GSE117865 https://www.ncbi.nlm.nih.gov/geo/query/acc.cgi?acc=GSE117865 and GSE46991 https://www.ncbi.nlm.nih.gov/geo/query/acc.cgi?acc=GSE46991. Bulk ATAC-seq profiles of RS4;11 cells were acquired from GEO GSE117865 and from bone marrow cell populations in Ulirsch et al 2019. Upon request additional information required to reanalyze the data reported in this paper is available from the lead contact.

ACKNOWLEDGEMENTS

The authors thank Professor Richard Lock (Children's Cancer Institute Australia) for providing PDX samples and related clinical information for this study. This research was funded by The Swedish Childhood Cancer Fund, the Swedish Cancer Society, The Swedish Research Council, Karolinska Institute, Radiumhemmets Research Foundation, AstraZeneca-SLL-KI Open Innovation grant (#18122013), the Academy of Finland (321553, 310106), ERA-NET ERA PerMed, Väre Foundation, Emil Aaltonen Foundation, Cancer Foundation Finland, Jane and Aatos Erkko foundation, Sigrid Juselius foundation, and the European Union Horizon 2020 research and innovation programme under grant agreement No 824110 (EASI-Genomics). The authors wish to acknowledge CSC – IT Center for Science, Finland and UEF Bioinformatics Center, University of Eastern Finland, Finland for computational resources. The authors would like to Acknowledge UEF Single Cell Genomics Core (Biocenter Finland), the Sequencing

Service GeneCore Sequencing Facility (EMBL, Heidelberg, Germany), SciLifeLab (Uppsala, Sweden) and Genome Center of Eastern Finland through providing sequencing services. The authors would like to Acknowledge Clinical Genomics Lund, SciLifeLab and Center for Translational Genomics (CTG), Lund University, for providing expertise and service with sequencing and analysis.

REFERENCES

Alkhatib, H., A. M. Rubinstein, S. Vasudevan, E. Flashner-Abramson, S. Stefansky, S. R. Chowdhury, S. Oguche, T. Peretz-Yablonsky, A. Granit, Z. Granot, I. Ben-Porath, K. Sheva, J. Feldman, N. E. Cohen, A. Meirovitz and N. Kravchenko-Balasha (2022). "Computational quantification and characterization of independently evolving cellular subpopulations within tumors is critical to inhibit anti-cancer therapy resistance." Genome Med **14**(1): 120.

Basu, B., E. Dean, M. Puglisi, A. Greystoke, M. Ong, W. Burke, M. Cavallin, G. Bigley, C. Womack, E. A. Harrington, S. Green, E. Oelmann, J. S. de Bono, M. Ranson and U. Banerji (2015). "First-in-Human Pharmacokinetic and Pharmacodynamic Study of the Dual m-TORC 1/2 Inhibitor AZD2014." Clin Cancer Res **21**(15): 3412-3419.

Bensinger, S. J., M. N. Bradley, S. B. Joseph, N. Zelcer, E. M. Janssen, M. A. Hausner, R. Shih, J. S. Parks, P. A. Edwards, B. D. Jamieson and P. Tontonoz (2008). "LXR signaling couples sterol metabolism to proliferation in the acquired immune response." Cell **134**(1): 97-111.

Bergen, V., M. Lange, S. Peidli, F. A. Wolf and F. J. Theis (2020). "Generalizing RNA velocity to transient cell states through dynamical modeling." Nat Biotechnol **38**(12): 1408-1414.

Bicocca, V. T., B. H. Chang, B. K. Masouleh, M. Muschen, M. M. Loriaux, B. J. Druker and J. W. Tyner (2012). "Crosstalk between ROR1 and the Pre-B cell receptor promotes survival of t(1;19) acute lymphoblastic leukemia." Cancer Cell **22**(5): 656-667.

Biggs, J. R., Y. Zhang, L. F. Peterson, M. Garcia, D. E. Zhang and A. S. Kraft (2005). "Phosphorylation of AML1/RUNX1 regulates its degradation and nuclear matrix association." Mol Cancer Res **3**(7): 391-401.

Cai, X., L. Gao, L. Teng, J. Ge, Z. M. Oo, A. R. Kumar, D. G. Gilliland, P. J. Mason, K. Tan and N. A. Speck (2015). "Runx1 Deficiency Decreases Ribosome Biogenesis and Confers Stress Resistance to Hematopoietic Stem and Progenitor Cells." Cell Stem Cell **17**(2): 165-177.

Carrassa, L. and G. Damia (2017). "DNA damage response inhibitors: Mechanisms and potential applications in cancer therapy." Cancer Treat Rev **60**: 139-151.

Chen, E. Y., C. M. Tan, Y. Kou, Q. Duan, Z. Wang, G. V. Meirelles, N. R. Clark and A. Ma'ayan (2013). "Enrichr: interactive and collaborative HTML5 gene list enrichment analysis tool." BMC Bioinformatics **14**: 128.

Cusanovich, D. A., A. J. Hill, D. Aghamirzaie, R. M. Daza, H. A. Pliner, J. B. Berletch, G. N. Filippova, X. Huang, L. Christiansen, W. S. DeWitt, C. Lee, S. G. Regalado, D. F. Read, F. J. Steemers, C. M. Disteche, C. Trapnell and J. Shendure (2018). "A Single-Cell Atlas of In Vivo Mammalian Chromatin Accessibility." Cell **174**(5): 1309-1324 e1318.

de Jong, M. R. W., M. Langendonk, B. Reitsma, P. Herbers, M. Nijland, G. Huls, A. van den Berg, E. Ammatuna, L. Visser and T. van Meerten (2019). "WEE1 Inhibition Enhances Anti-

Apoptotic Dependency as a Result of Premature Mitotic Entry and DNA Damage." Cancers (Basel) **11**(11).
Ebinger, S., E. Z. Ozdemir, C. Ziegenhain, S. Tiedt, C. Castro Alves, M. Grunert, M. Dworzak, C. Lutz, V. A. Turati, T. Enver, H. P. Horny, K. Sotlar, S. Parekh, K. Spiekermann, W. Hiddemann, A. Schepers, B. Polzer, S. Kirsch, M. Hoffmann, B. Knapp, J. Hasenauer, H. Pfeifer, R. Panzer-Grumayer, W. Enard, O. Gires and I. Jeremias (2016). "Characterization of Rare, Dormant, and Therapy-Resistant Cells in Acute Lymphoblastic Leukemia." Cancer Cell **30**(6): 849-862.
Elbaek, C. R., V. Petrosius, J. Benada, L. Erichsen, R. B. Damgaard and C. S. Sorensen (2022). "WEE1 kinase protects the stability of stalled DNA replication forks by limiting CDK2 activity." Cell Rep **38**(3): 110261.
Elbaek, C. R., V. Petrosius and C. S. Sorensen (2020). "WEE1 kinase limits CDK activities to safeguard DNA replication and mitotic entry." Mutat Res **819-820**: 111694.
Friedman, A. D. (2009). "Cell cycle and developmental control of hematopoiesis by Runx1." J Cell Physiol **219**(3): 520-524.
Fu, S., Y. Wang, K. Keyomarsi, F. Meric-Bernstam and F. Meric-Bernstein (2018). "Strategic development of AZD1775, a Wee1 kinase inhibitor, for cancer therapy." Expert Opin Investig Drugs **27**(9): 741-751.
Geng, H., C. Hurtz, K. B. Lenz, Z. Chen, D. Baumjohann, S. Thompson, N. A. Goloviznina, W. Y. Chen, J. Huan, D. LaTocha, E. Ballabio, G. Xiao, J. W. Lee, A. Deucher, Z. Qi, E. Park, C. Huang, R. Nahar, S. M. Kweon, S. Shojaee, L. N. Chan, J. Yu, S. M. Kornblau, J. J. Bijl, B. H. Ye, K. M. Ansel, E. Paietta, A. Melnick, S. P. Hunger, P. Kurre, J. W. Tyner, M. L. Loh, R. G. Roeder, B. J. Druker, J. A. Burger, T. A. Milne, B. H. Chang and M. Muschen (2015). "Self-enforcing feedback activation between BCL6 and pre-B cell receptor signaling defines a distinct subtype of acute lymphoblastic leukemia." Cancer Cell **27**(3): 409-425.
Ghelli Luserna Di Rora, A., N. Beeharry, E. Imbrogno, A. Ferrari, V. Robustelli, S. Righi, E. Sabattini, M. V. Verga Falzacappa, C. Ronchini, N. Testoni, C. Baldazzi, C. Papayannidis, M. C. Abbenante, G. Marconi, S. Paolini, S. Parisi, C. Sartor, M. C. Fontana, S. De Matteis, I. Iacobucci, P. G. Pelicci, M. Cavo, T. J. Yen and G. Martinelli (2018). "Targeting WEE1 to enhance conventional therapies for acute lymphoblastic leukemia." J Hematol Oncol **11**(1): 99.
Guenther, M. G., L. N. Lawton, T. Rozovskaia, G. M. Frampton, S. S. Levine, T. L. Volkert, C. M. Croce, T. Nakamura, E. Canaani and R. A. Young (2008). "Aberrant chromatin at genes encoding stem cell regulators in human mixed-lineage leukemia." Genes Dev **22**(24): 3403-3408.
Guo, E., R. Xiao, Y. Wu, F. Lu, C. Liu, B. Yang, X. Li, Y. Fu, Z. Wang, Y. Li, Y. Huang, F. Li, X. Wu, L. You, T. Qin, Y. Lu, X. Huang, D. Ma, G. B. Mills, C. Sun and G. Chen (2022). "WEE1 inhibition induces anti-tumor immunity by activating ERV and the dsRNA pathway." J Exp Med **219**(1).
Harman, J. R., R. Thorne, M. Jamilly, M. Tapia, N. T. Crump, S. Rice, R. Beveridge, E. Morrissey, M. de Bruijn, I. Roberts, A. Roy, T. A. Fulga and T. A. Milne (2021). "A KMT2A-AFF1 gene regulatory network highlights the role of core transcription factors and reveals the regulatory logic of key downstream target genes." Genome Res **31**(7): 1159-1173.
Heinaniemi, M., T. Vuorenmaa, S. Teppo, M. U. Kaikkonen, M. Bouvy-Liivrand, J. Mehtonen, H. Niskanen, V. Zachariadis, S. Laukkanen, T. Liuksiala, K. Teittinen and O. Lohi (2016). "Transcription-coupled genetic instability marks acute lymphoblastic leukemia structural variation hotspots." Elife **5**.
Heinz, S., C. Benner, N. Spann, E. Bertolino, Y. C. Lin, P. Laslo, J. X. Cheng, C. Murre, H. Singh and C. K. Glass (2010). "Simple combinations of lineage-determining transcription factors prime cis-regulatory elements required for macrophage and B cell identities." Mol Cell **38**(4): 576-589.

Hirai, H., Y. Iwasawa, M. Okada, T. Arai, T. Nishibata, M. Kobayashi, T. Kimura, N. Kaneko, J. Ohtani, K. Yamanaka, H. Itadani, I. Takahashi-Suzuki, K. Fukasawa, H. Oki, T. Nambu, J. Jiang, T. Sakai, H. Arakawa, T. Sakamoto, T. Sagara, T. Yoshizumi, S. Mizuarai and H. Kotani (2009). "Small-molecule inhibition of Wee1 kinase by MK-1775 selectively sensitizes p53-deficient tumor cells to DNA-damaging agents." Mol Cancer Ther **8**(11): 2992-3000.
Hurtz, C., L. N. Chan, H. Geng, E. Ballabio, G. Xiao, G. Deb, H. Khoury, C. W. Chen, S. A. Armstrong, J. Chen, P. Ernst, A. Melnick, T. Milne and M. Muschen (2019). "Rationale for targeting BCL6 in MLL-rearranged acute lymphoblastic leukemia." Genes Dev **33**(17-18): 1265-1279.
Kamisuki, S., Q. Mao, L. Abu-Elheiga, Z. Gu, A. Kugimiya, Y. Kwon, T. Shinohara, Y. Kawazoe, S. Sato, K. Asakura, H. Y. Choo, J. Sakai, S. J. Wakil and M. Uesugi (2009). "A small molecule that blocks fat synthesis by inhibiting the activation of SREBP." Chem Biol **16**(8): 882-892.
Khabirova, E., L. Jardine, T. H. H. Coorens, S. Webb, T. D. Treger, J. Engelbert, T. Porter, E. Prigmore, G. Collord, A. Piapi, S. A. Teichmann, S. Inglott, O. Williams, O. Heidenreich, M. D. Young, K. Straathof, S. Bomken, J. Bartram, M. Haniffa and S. Behjati (2022). "Single-cell transcriptomics reveals a distinct developmental state of KMT2A-rearranged infant B-cell acute lymphoblastic leukemia." Nat Med **28**(4): 743-751.
Kim, E., C. Hurtz, S. Koehrer, Z. Wang, S. Balasubramanian, B. Y. Chang, M. Muschen, R. E. Davis and J. A. Burger (2017). "Ibrutinib inhibits pre-BCR(+) B-cell acute lymphoblastic leukemia progression by targeting BTK and BLK." Blood **129**(9): 1155-1165.
Knoechel, B., J. E. Roderick, K. E. Williamson, J. Zhu, J. G. Lohr, M. J. Cotton, S. M. Gillespie, D. Fernandez, M. Ku, H. Wang, F. Piccioni, S. J. Silver, M. Jain, D. Pearson, M. J. Kluk, C. J. Ott, L. D. Shultz, M. A. Brehm, D. L. Greiner, A. Gutierrez, K. Stegmaier, A. L. Kung, D. E. Root, J. E. Bradner, J. C. Aster, M. A. Kelliher and B. E. Bernstein (2014). "An epigenetic mechanism of resistance to targeted therapy in T cell acute lymphoblastic leukemia." Nat Genet **46**(4): 364-370.
Kong, A. and H. Mehanna (2021). "WEE1 Inhibitor: Clinical Development." Curr Oncol Rep **23**(9): 107.
Kuleshov, M. V., M. R. Jones, A. D. Rouillard, N. F. Fernandez, Q. Duan, Z. Wang, S. Koplev, S. L. Jenkins, K. M. Jagodnik, A. Lachmann, M. G. McDermott, C. D. Monteiro, G. W. Gundersen and A. Ma'ayan (2016). "Enrichr: a comprehensive gene set enrichment analysis web server 2016 update." Nucleic Acids Res **44**(W1): W90-97.
La Manno, G., R. Soldatov, A. Zeisel, E. Braun, H. Hochgerner, V. Petukhov, K. Lidschreiber, M. E. Kastriti, P. Lonnerberg, A. Furlan, J. Fan, L. E. Borm, Z. Liu, D. van Bruggen, J. Guo, X. He, R. Barker, E. Sundstrom, G. Castelo-Branco, P. Cramer, I. Adameyko, S. Linnarsson and P. V. Kharchenko (2018). "RNA velocity of single cells." Nature **560**(7719): 494-498.
Langmead, B., M. C. Schatz, J. Lin, M. Pop and S. L. Salzberg (2009). "Searching for SNPs with cloud computing." Genome Biol **10**(11): R134.
Liedtke, M. and M. L. Cleary (2009). "Therapeutic targeting of MLL." Blood **113**(24): 6061-6068.
Liu, H., S. Takeda, R. Kumar, T. D. Westergard, E. J. Brown, T. K. Pandita, E. H. Cheng and J. J. Hsieh (2010). "Phosphorylation of MLL by ATR is required for execution of mammalian S-phase checkpoint." Nature **467**(7313): 343-346.
Lock, R. B., N. Liem, M. L. Farnsworth, C. G. Milross, C. Xue, M. Tajbakhsh, M. Haber, M. D. Norris, G. M. Marshall and A. M. Rice (2002). "The nonobese diabetic/severe combined immunodeficient (NOD/SCID) mouse model of childhood acute lymphoblastic leukemia reveals intrinsic differences in biologic characteristics at diagnosis and relapse." Blood **99**(11): 4100-4108.

Mahajan, K. and N. P. Mahajan (2013). "WEE1 tyrosine kinase, a novel epigenetic modifier." Trends Genet **29**(7): 394-402.
McGowan, C. H. and P. Russell (1995). "Cell cycle regulation of human WEE1." EMBO J **14**(10): 2166-2175.
Mehtonen, J., S. Teppo, M. Lahnalampi, A. Kokko, R. Kaukonen, L. Oksa, M. Bouvy-Liivrand, A. Malyukova, A. Makinen, S. Laukkanen, P. I. Makinen, S. Rounioja, P. Ruusuvuori, O. Sangfelt, R. Lund, T. Lonnberg, O. Lohi and M. Heinaniemi (2020). "Single cell characterization of B-lymphoid differentiation and leukemic cell states during chemotherapy in ETV6-RUNX1-positive pediatric leukemia identifies drug-targetable transcription factor activities." Genome Med **12**(1): 99.
Meyer, C., E. Kowarz, J. Hofmann, A. Renneville, J. Zuna, J. Trka, R. Ben Abdelali, E. Macintyre, E. De Braekeleer, M. De Braekeleer, E. Delabesse, M. P. de Oliveira, H. Cave, E. Clappier, J. J. van Dongen, B. V. Balgobind, M. M. van den Heuvel-Eibrink, H. B. Beverloo, R. Panzer-Grumayer, A. Teigler-Schlegel, J. Harbott, E. Kjeldsen, S. Schnittger, U. Koehl, B. Gruhn, O. Heidenreich, L. C. Chan, S. F. Yip, M. Krzywinski, C. Eckert, A. Moricke, M. Schrappe, C. N. Alonso, B. W. Schafer, J. Krauter, D. A. Lee, U. Zur Stadt, G. Te Kronnie, R. Sutton, S. Izraeli, L. Trakhtenbrot, L. Lo Nigro, G. Tsaur, L. Fechina, T. Szczepanski, S. Strehl, D. Ilencikova, M. Molkentin, T. Burmeister, T. Dingermann, T. Klingebiel and R. Marschalek (2009). "New insights to the MLL recombinome of acute leukemias." Leukemia **23**(8): 1490-1499.
Moiseeva, T. N., C. Qian, N. Sugitani, H. U. Osmanbeyoglu and C. J. Bakkenist (2019). "WEE1 kinase inhibitor AZD1775 induces CDK1 kinase-dependent origin firing in unperturbed G1- and S-phase cells." Proc Natl Acad Sci U S A **116**(48): 23891-23893.
Parker, L. L., P. J. Sylvestre, M. J. Byrnes, 3rd, F. Liu and H. Piwnica-Worms (1995). "Identification of a 95-kDa WEE1-like tyrosine kinase in HeLa cells." Proc Natl Acad Sci U S A **92**(21): 9638-9642.
Phan, R. T. and R. Dalla-Favera (2004). "The BCL6 proto-oncogene suppresses p53 expression in germinal-centre B cells." Nature **432**(7017): 635-639.
Polonen, P., J. Mehtonen, J. Lin, T. Liuksiala, S. Hayrynen, S. Teppo, A. Makinen, A. Kumar, D. Malani, V. Pohjolainen, K. Porkka, C. A. Heckman, P. May, V. Hautamaki, K. J. Granberg, O. Lohi, M. Nykter and M. Heinaniemi (2019). "Hemap: An Interactive Online Resource for Characterizing Molecular Phenotypes across Hematologic Malignancies." Cancer Res **79**(10): 2466-2479.
Ranuncolo, S. M., J. M. Polo and A. Melnick (2008). "BCL6 represses CHEK1 and suppresses DNA damage pathways in normal and malignant B-cells." Blood Cells Mol Dis **41**(1): 95-99.
Richmond, J., H. Carol, K. Evans, L. High, A. Mendomo, A. Robbins, C. Meyer, N. C. Venn, R. Marschalek, M. Henderson, R. Sutton, R. T. Kurmasheva, U. R. Kees, P. J. Houghton, M. A. Smith and R. B. Lock (2015). "Effective targeting of the P53-MDM2 axis in preclinical models of infant MLL-rearranged acute lymphoblastic leukemia." Clin Cancer Res **21**(6): 1395-1405.
Ricoult, S. J., J. L. Yecies, I. Ben-Sahra and B. D. Manning (2016). "Oncogenic PI3K and K-Ras stimulate de novo lipid synthesis through mTORC1 and SREBP." Oncogene **35**(10): 1250-1260.
Russell, P. and P. Nurse (1987). "Negative regulation of mitosis by wee1+, a gene encoding a protein kinase homolog." Cell **49**(4): 559-567.
Schep, A. N., B. Wu, J. D. Buenrostro and W. J. Greenleaf (2017). "chromVAR: inferring transcription-factor-associated accessibility from single-cell epigenomic data." Nat Methods **14**(10): 975-978.
Sicklick, J. K., S. Kato, R. Okamura, H. Patel, M. Nikanjam, P. T. Fanta, M. E. Hahn, P. De, C. Williams, J. Guido, B. M. Solomon, R. R. McKay, A. Krie, S. G. Boles, J. S. Ross, J. J. Lee,

B. Leyland-Jones, S. M. Lippman and R. Kurzrock (2021). "Molecular profiling of advanced malignancies guides first-line N-of-1 treatments in the I-PREDICT treatment-naive study." Genome Med **13**(1): 155.
Sorensen, C. S. and R. G. Syljuasen (2012). "Safeguarding genome integrity: the checkpoint kinases ATR, CHK1 and WEE1 restrain CDK activity during normal DNA replication." Nucleic Acids Res **40**(2): 477-486.
Stuart, T., A. Butler, P. Hoffman, C. Hafemeister, E. Papalexi, W. M. Mauck, 3rd, Y. Hao, M. Stoeckius, P. Smibert and R. Satija (2019). "Comprehensive Integration of Single-Cell Data." Cell **177**(7): 1888-1902 e1821.
Takebe, N., G. H. O. S. Coyne, S. Kummar, K. T. Do, A. Bruns, L. Juwara, M. F. Quinn, L. Harris, R. Piekarz, S. A. Prindiville, E. Sharon, H. Streicher, G. Mugundu, J. J. Ji, D. Wilsker, R. J. Kinders, L. Rubinstein, J. H. Doroshow and A. P. Chen (2018). "Safety, tolerability, and antitumor activity of once-daily Wee-1 inhibitor AZD1775." Journal of Clinical Oncology **36**(15_suppl): 2587-2587.
Taniguchi, H., R. Caeser, S. S. Chavan, Y. A. Zhan, A. Chow, P. Manoj, F. Uddin, H. Kitai, R. Qu, O. Hayatt, N. S. Shah, A. Quintanal Villalonga, V. Allaj, E. M. Nguyen, J. Chan, A. O. Michel, H. Mukae, E. de Stanchina, C. M. Rudin and T. Sen (2022). "WEE1 inhibition enhances the antitumor immune response to PD-L1 blockade by the concomitant activation of STING and STAT1 pathways in SCLC." Cell Rep **39**(7): 110814.
Tay, L. S., V. Krishnan, H. Sankar, Y. L. Chong, L. S. H. Chuang, T. Z. Tan, A. M. Kolinjivadi, D. Kappei and Y. Ito (2018). "RUNX Poly(ADP-Ribosyl)ation and BLM Interaction Facilitate the Fanconi Anemia Pathway of DNA Repair." Cell Rep **24**(7): 1747-1755.
Tsuzuki, S., T. Yasuda, S. Kojima, M. Kawazu, K. Akahane, T. Inukai, M. Imaizumi, T. Morishita, K. Miyamura, T. Ueno, S. Karnan, A. Ota, T. Hyodo, H. Konishi, M. Sanada, H. Nagai, K. Horibe, A. Tomita, K. Suzuki, H. Muramatsu, Y. Takahashi, Y. Miyazaki, I. Matsumura, H. Kiyoi, Y. Hosokawa, H. Mano and F. Hayakawa (2020). "Targeting MEF2D-fusion Oncogenic Transcriptional Circuitries in B-cell Precursor Acute Lymphoblastic Leukemia." Blood Cancer Discov **1**(1): 82-95.
van Galen, P., V. Hovestadt, M. H. Wadsworth Ii, T. K. Hughes, G. K. Griffin, S. Battaglia, J. A. Verga, J. Stephansky, T. J. Pastika, J. Lombardi Story, G. S. Pinkus, O. Pozdnyakova, I. Galinsky, R. M. Stone, T. A. Graubert, A. K. Shalek, J. C. Aster, A. A. Lane and B. E. Bernstein (2019). "Single-Cell RNA-Seq Reveals AML Hierarchies Relevant to Disease Progression and Immunity." Cell **176**(6): 1265-1281 e1224.
Wang, S., Y. Zhang, J. Soosairajah and A. S. Kraft (2007). "Regulation of RUNX1/AML1 during the G2/M transition." Leuk Res **31**(6): 839-851.
Watanabe, N., H. Arai, J. Iwasaki, M. Shiina, K. Ogata, T. Hunter and H. Osada (2005). "Cyclin-dependent kinase (CDK) phosphorylation destabilizes somatic Wee1 via multiple pathways." Proc Natl Acad Sci U S A **102**(33): 11663-11668.
Webster, G. A. and N. D. Perkins (1999). "Transcriptional cross talk between NF-kappaB and p53." Mol Cell Biol **19**(5): 3485-3495.
Wilkinson, A. C., E. Ballabio, H. Geng, P. North, M. Tapia, J. Kerry, D. Biswas, R. G. Roeder, C. D. Allis, A. Melnick, M. F. de Bruijn and T. A. Milne (2013). "RUNX1 is a key target in t(4;11) leukemias that contributes to gene activation through an AF4-MLL complex interaction." Cell Rep **3**(1): 116-127.
Winters, A. C. and K. M. Bernt (2017). "MLL-Rearranged Leukemias-An Update on Science and Clinical Approaches." Front Pediatr **5**: 4.
Wray, J. P., E. M. Deltcheva, C. Boiers, C. Richardson Scapital Ie, J. B. Chhetri, J. Brown, S. Gagrica, Y. Guo, A. Illendula, J. H. A. Martens, H. G. Stunnenberg, J. H. Bushweller, R. Nimmo and T. Enver (2022). "Regulome analysis in B-acute lymphoblastic leukemia exposes Core Binding Factor addiction as a therapeutic vulnerability." Nat Commun **13**(1): 7124.

Ford, J. B., D. Baturin, T. M. Burleson, A. A. Van Linden, Y. M. Kim and C. C. Porter (2015). "AZD1775 sensitizes T cell acute lymphoblastic leukemia cells to cytarabine by promoting apoptosis over DNA repair." Oncotarget **6**(29): 28001-28010.
Garcia, T. B., J. C. Snedeker, D. Baturin, L. Gardner, S. P. Fosmire, C. Zhou, C. T. Jordan, S. Venkataraman, R. Vibhakar and C. C. Porter (2017). "A Small-Molecule Inhibitor of WEE1, AZD1775, Synergizes with Olaparib by Impairing Homologous Recombination and Enhancing DNA Damage and Apoptosis in Acute Leukemia." Mol Cancer Ther **16**(10): 2058-2068.
Heinäniemi, M., T. Vuorenmaa, S. Teppo, M. U. Kaikkonen, M. Bouvy-Liivrand, J. Mehtonen, H. Niskanen, V. Zachariadis, S. Laukkanen, T. Liuksiala, K. Teittinen and O. Lohi (2016). "Transcription-coupled genetic instability marks acute lymphoblastic leukemia structural variation hotspots." Elife **5**.
Petrosius, V., J. Benada, O. Nielsen, E. M. Schoof and C. S. Sorensen (2023). "Temporal phosphoproteomics reveals WEE1-dependent control of 53BP1 pathway." iScience **26**(1): 105806.
Tibes, R., J. M. Bogenberger, L. Chaudhuri, R. T. Hagelstrom, D. Chow, M. E. Buechel, I. M. Gonzales, T. Demuth, J. Slack, R. A. Mesa, E. Braggio, H. H. Yin, S. Arora and D. O. Azorsa (2012). "RNAi screening of the kinome with cytarabine in leukemias." Blood **119**(12): 2863-2872.
Van Linden, A. A., D. Baturin, J. B. Ford, S. P. Fosmire, L. Gardner, C. Korch, P. Reigan and C. C. Porter (2013). "Inhibition of Wee1 sensitizes cancer cells to antimetabolite chemotherapeutics in vitro and in vivo, independent of p53 functionality." Mol Cancer Ther **12**(12): 2675-2684.
Wray, J. P., E. M. Deltcheva, C. Boiers, C. Richardson Scapital Ie, J. B. Chhetri, J. Brown, S. Gagrica, Y. Guo, A. Illendula, J. H. A. Martens, H. G. Stunnenberg, J. H. Bushweller, R. Nimmo and T. Enver (2022). "Regulome analysis in B-acute lymphoblastic leukemia exposes Core Binding Factor addiction as a therapeutic vulnerability." Nat Commun **13**(1): 7124.
Andersson, A. K., J. Ma, J. Wang, X. Chen, A. L. Gedman, J. Dang, J. Nakitandwe, L. Holmfeldt, M. Parker, J. Easton, R. Huether, R. Kriwacki, M. Rusch, G. Wu, Y. Li, H. Mulder, S. Raimondi, S. Pounds, G. Kang, L. Shi, J. Becksfort, P. Gupta, D. Payne-Turner, B. Vadodaria, K. Boggs, D. Yergeau, J. Manne, G. Song, M. Edmonson, P. Nagahawatte, L. Wei, C. Cheng, D. Pei, R. Sutton, N. C. Venn, A. Chetcuti, A. Rush, D. Catchpoole, J. Heldrup, T. Fioretos, C. Lu, L. Ding, C. H. Pui, S. Shurtleff, C. G. Mullighan, E. R. Mardis, R. K. Wilson, T. A. Gruber, J. Zhang, J. R. Downing and P. St. Jude Children's Research Hospital-Washington University Pediatric Cancer Genome (2015). "The landscape of somatic mutations in infant MLL-rearranged acute lymphoblastic leukemias." Nat Genet **47**(4): 330-337.
Chan, A. K. N. and C. W. Chen (2019). "Rewiring the Epigenetic Networks in MLL-Rearranged Leukemias: Epigenetic Dysregulation and Pharmacological Interventions." Front Cell Dev Biol **7**: 81.
Chen, C., W. Yu, F. Alikarami, Q. Qiu, C. H. Chen, J. Flournoy, P. Gao, Y. Uzun, L. Fang, J. W. Davenport, Y. Hu, Q. Zhu, K. Wang, C. Libbrecht, A. Felmeister, I. Rozich, Y. Y. Ding, S. P. Hunger, C. A. Felix, H. Wu, P. A. Brown, E. M. Guest, D. M. Barrett, K. M. Bernt and K. Tan (2022). "Single-cell multiomics reveals increased plasticity, resistant populations, and stem-cell-like blasts in KMT2A-rearranged leukemia." Blood **139**(14): 2198-2211.
O'Connor, M. J. (2015). "Targeting the DNA Damage Response in Cancer." Mol Cell **60**(4): 547-560.

Okada, Y., Q. Feng, Y. Lin, Q. Jiang, Y. Li, V. M. Coffield, L. Su, G. Xu and Y. Zhang (2005). "hDOT1L links histone methylation to leukemogenesis." Cell **121**(2): 167-178.
Tsuzuki, S., T. Yasuda, S. Kojima, M. Kawazu, K. Akahane, T. Inukai, M. Imaizumi, T. Morishita, K. Miyamura, T. Ueno, S. Karnan, A. Ota, T. Hyodo, H. Konishi, M. Sanada, H. Nagai, K. Horibe, A. Tomita, K. Suzuki, H. Muramatsu, Y. Takahashi, Y. Miyazaki, I. Matsumura, H. Kiyoi, Y. Hosokawa, H. Mano and F. Hayakawa (2020). "Targeting MEF2D-fusion Oncogenic Transcriptional Circuitries in B-cell Precursor Acute Lymphoblastic Leukemia." Blood Cancer Discov **1**(1): 82-95.
Visconti, R., R. Della Monica, L. Palazzo, F. D'Alessio, M. Raia, S. Improta, M. R. Villa, L. Del Vecchio and D. Grieco (2015). "The Fcp1-Wee1-Cdk1 axis affects spindle assembly checkpoint robustness and sensitivity to antimicrotubule cancer drugs." Cell Death Differ **22**(9): 1551-1560.

Figure 1

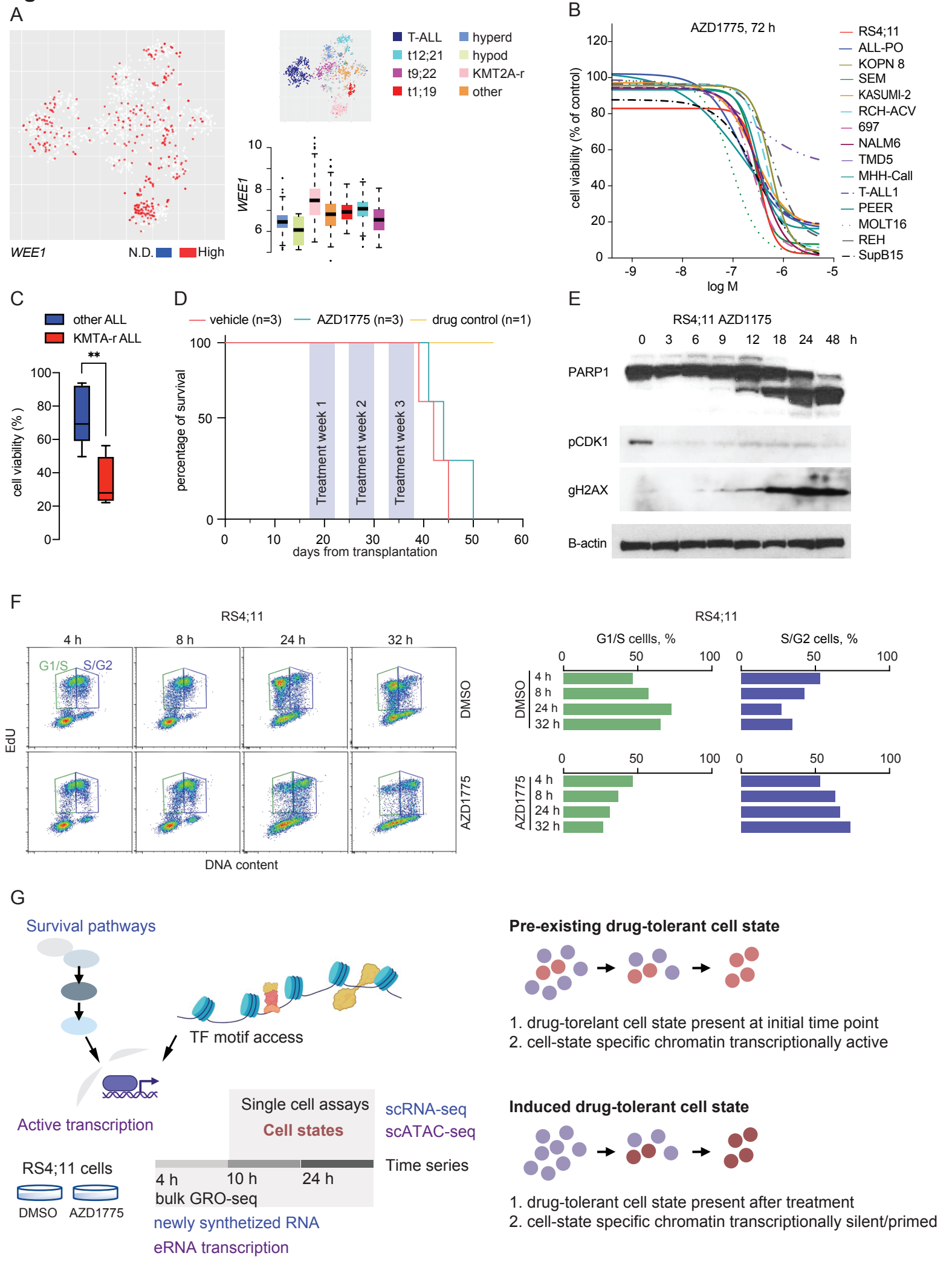
A
WEE1
N.D.
High
T-ALL
t12;21
t9;22
t1;19
hyperd
hypod
KMT2A-r
other
WEE1
B
AZD1775, 72 h
cell viability (% of control)
log M
RS4;11
ALL-PO
KOPN 8
SEM
KASUMI-2
RCH-ACV
697
NALM6
TMD5
MHH-Call
T-ALL1
PEER
MOLT16
REH
SupB15
C
other ALL
KMTA-r ALL
cell viability (%)
D
vehicle (n=3)
AZD1775 (n=3)
drug control (n=1)
percentage of survival
Treatment week 1
Treatment week 2
Treatment week 3
days from transplantation
E
RS4;11 AZD1175
PARP1
pCDK1
gH2AX
B-actin
F
RS4;11
4 h
8 h
24 h
32 h
G1/S
S/G2
EdU
DMSO
AZD1775
DNA content
G1/S cellls, %
S/G2 cells, %
G
Survival pathways
TF motif access
Active transcription
Single cell assays
Cell states
scRNA-seq
scATAC-seq
Time series
RS4;11 cells
DMSO
AZD1775
4 h
10 h
24 h
bulk GRO-seq
newly synthetized RNA
eRNA transcription
Pre-existing drug-tolerant cell state
1. drug-torelant cell state present at initial time point
2. cell-state specific chromatin transcriptionally active
Induced drug-tolerant cell state
1. drug-tolerant cell state present after treatment
2. cell-state specific chromatin transcriptionally silent/primed

Figure 1. AZD1775 response profiling reveals dependency on WEE1 in KTM2A-r ALLs *in vitro* and emergence of drug tolerance in a monotherapy setting *in vivo*.

A. WEE1 gene expression in primary ALL samples in HEMAP. tSNE-map: low (in white) vs high (in red) mRNA level is visualized for each patient transcriptome profile. Boxplot: normalized gene expression level comparing across subtypes. Subtype annotation is indicated by different colors (right panel).

B. AZD1775 dose response profiles (relative to DMSO control) were assessed by Alamar Blue assay in T-ALL1, Molt16, Peer, RCH-ACV, 697, Kasumi-2, MHH-Call3, SupB15, TMD6, Nalm-6, REH, RS4;11, SEM and KOPN8 ALL cells. Percentage of viable cells after 72 h treatment with increasing concentrations of AZD1775 is shown.

C. Recovery of proliferation following removal of AZD1775 (relative to DMSO) analysed by Alamar Blue assay. Cell lines were treated for three days with AZD1775 (corresponding IC50 for each cell line, please see Fig S1B) and allowed to recover for an additional 14 days without the drug. Box plot comparing recovery in KMT2A-r and non-KMT2A-r ALL cell lines (corresponding subtypes TCF3-PBX1, ETV6-RUNX1, TCF3-PDGFRB) is shown. ** denotes p=0.0086 determined using t-test. Data are represented as mean ± SD.

D. Kaplan-Meier survival curves of MLL-7 patient cells treated in a xenograft model with AZD1775.

E. Cellular response to AZD1775 (600 nM) in KMT2A-r RS4;11 cells was assessed at the indicated time points by Western blot analysis. Whole cell lysates were immunoblotted with the specified antibodies; Cleaved PARP1 (marker of cell death), phosphorylation of CDK1-Y15 (marker of WEE1 inhibition) and phosphorylation of γH2AX-S139 (marker for DNA damage). β-actin was used as a loading control.

F. Flow cytometry density plots showing distribution of EdU (replicating cells, Y-axes) and DNA content (Propidium Iodide, PI, X-axes) to determine G1/S (green) and S/G2M (purple) proportions. RS4;11 cells were pulse-labelled for 30 minutes with EdU, treated with DMSO or AZD1775 (600 nM) and chased for the times indicated.

G. Overview of the experimental setup for genomics characterization of early drug response dynamics using GRO-, scRNA-, and scATAC-seq to distinguish pre-existing and induced drug tolerance. Time series (4, 10 and 24 h treatment) in GRO-seq coupled with cellular resolution single cell genomics assays at 10 and 24 h to detect drug-tolerant cell states and decipher their corresponding survival pathway and regulatory network activity.

Figure 2

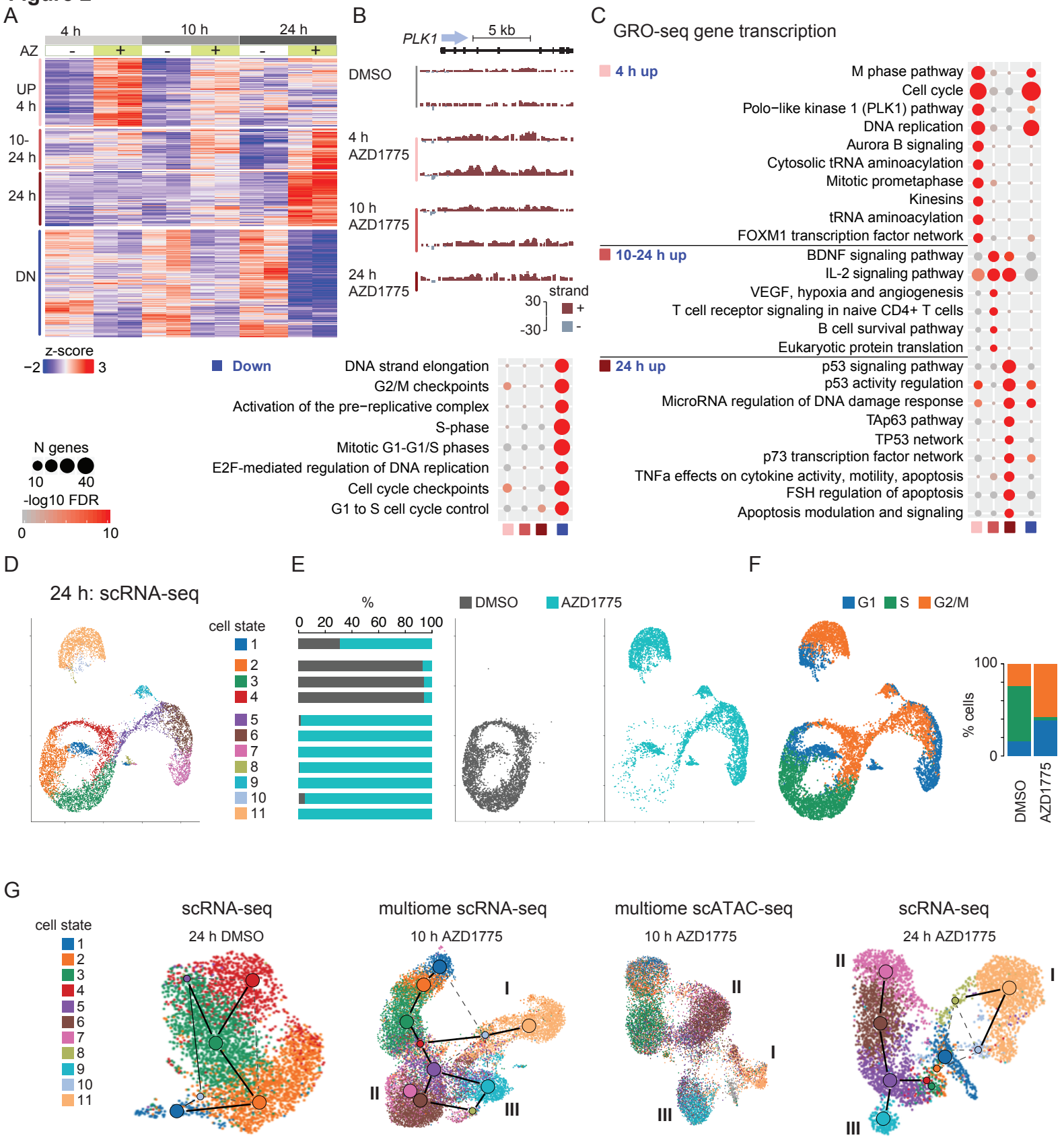
A
4 h
10 h
24 h
AZ
-
+
UP 4 h
10-24 h
24 h
DN
z-score
−2
3
Down
B
PLK1
5 kb
DMSO
4 h AZD1775
10 h AZD1775
24 h AZD1775
strand
30
-30
+
-
C
GRO-seq gene transcription
4 h up
M phase pathway
Cell cycle
Polo−like kinase 1 (PLK1) pathway
DNA replication
Aurora B signaling
Cytosolic tRNA aminoacylation
Mitotic prometaphase
Kinesins
tRNA aminoacylation
FOXM1 transcription factor network
10-24 h up
BDNF signaling pathway
IL-2 signaling pathway
VEGF, hypoxia and angiogenesis
T cell receptor signaling in naive CD4+ T cells
B cell survival pathway
Eukaryotic protein translation
24 h up
p53 signaling pathway
p53 activity regulation
MicroRNA regulation of DNA damage response
TAp63 pathway
TP53 network
p73 transcription factor network
TNFa effects on cytokine activity, motility, apoptosis
FSH regulation of apoptosis
Apoptosis modulation and signaling
DNA strand elongation
G2/M checkpoints
Activation of the pre−replicative complex
S-phase
Mitotic G1-G1/S phases
E2F-mediated regulation of DNA replication
Cell cycle checkpoints
G1 to S cell cycle control
N genes
10
40
-log10 FDR
0
10
D
24 h: scRNA-seq
cell state
1
2
3
4
5
6
7
8
9
10
11
E
%
0
20
40
60
80
100
DMSO
AZD1775
F
G1
S
G2/M
100
0
% cells
DMSO
AZD1775
G
cell state
1
2
3
4
5
6
7
8
9
10
11
scRNA-seq
24 h DMSO
multiome scRNA-seq
10 h AZD1775
multiome scATAC-seq
10 h AZD1775
scRNA-seq
24 h AZD1775
I
II
III

Figure 2. WEE1 kinase inhibition triggers a rapid transcriptional response and emergence of multiple cell states.

A. Heatmap illustrating the magnitude and direction of changes in the GRO-seq signal (z-score; tones of red indicate high level, tones of blue low level) for annotated gene transcripts. Gene clusters that correspond to regulation patterns 4 h up, 10-24 h up, 24 h up, and down are shown.

B. GRO-seq signal is illustrated at *PLK1* gene region from replicate samples collected at 4, 10 and 24 h (top left). Signal from +/- stand is plotted above (in red) or below (in grey), respectively.

C. Enrichment of biological processes for GRO-seq gene clusters (right: upregulated with distinct time profile, left: downregulated) shown as dot plots. Size of the dot corresponds to the number of genes from the gene set and -log10 FDR value is shown in color.

D-F. Low dimensional projection and scRNA-seq transcriptome-based clustering for the RS4;11 cells from DMSO and AZD1775 treated cells are shown on the UMAP visualization. Colors correspond to cell state assignment (in D), treatment (in E), and assigned cell cycle status (F). Quantification of cell proportions across categories is shown in E and F.

G. Low dimensional projections based on transcriptome and chromatin access profiles are shown in UMAPs generated separately for DMSO and AZD1175 treated cells. Graph connectivity (PAGA) is visualized on scRNA-seq maps where connecting lines indicate putative cell state transition paths. Multiome data from 10 h includes scATAC-seq from the same cells. The colors correspond to assigned cell state based on 24 h scRNA-seq data, refer to cell states shown in D. Three treatment-specific cell fates that are reproducibly found in both time points and data modalities are indicated by roman numerals.

Figure 3

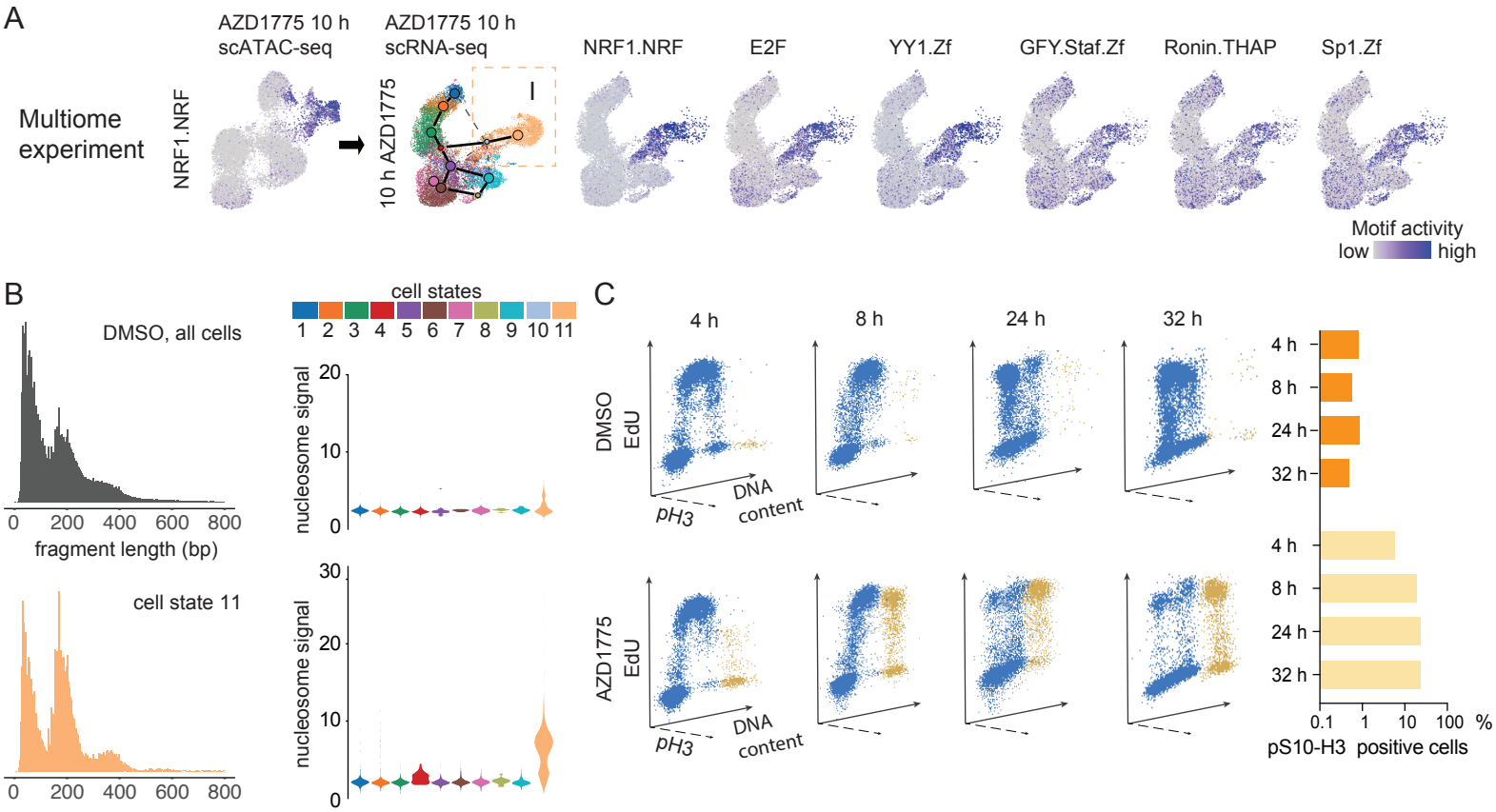
A
AZD1775 10 h
scATAC-seq
AZD1775 10 h
scRNA-seq
NRF1.NRF
E2F
YY1.Zf
GFY.Staf.Zf
Ronin.THAP
Sp1.Zf
Multiome
experiment
NRF1.NRF
10 h AZD1775
I
Motif activity
low
high
B
DMSO, all cells
fragment length (bp)
cell state 11
cell states
1 2 3 4 5 6 7 8 9 10 11
nucleosome signal
C
4 h
8 h
24 h
32 h
DMSO
EdU
AZD1775
EdU
pH3
DNA
content
pS10-H3 positive cells
%

Figure 3. Forced mitotic entry in response to AZD1775 treatment arrests cells from S-phase in a condensed mitotic-like chromatin state.

A. TF motif activity (ChromVar) is shown for TFs with highest motif access in cell fate I (highlighted, refer also to Fig. S2G). The corresponding TF motif activity for all TF motifs derived from scATAC-seq is visualized on the 10 h scRNA-seq UMAP from the 10 h multiome profile. NRF1 motif with highest cluster-specific activity (summarized in Table S3) is shown on scATAC-seq UMAP (10 h). Darker tones correspond to high motif access.

B. scATAC 24h DMSO DNA fragment length distribution (DMSO-treated cells top left) and cell state 11 (bottom left) compared in density plots (left). The nucleosome signal metric calculated from the ratio of fragments between 147 bp and 294 bp (mononucleosome) to fragments < 147 bp (nucleosome-free) compared across cell states is shown as violin plots (right panel, top: DMSO, bottom AZD1775-treated cells).

C. 3D flow cytometry dot plots showing the distribution of EdU (replicating cells, Y-axes) versus DNA content (X-axes). RS4;11 cells were pulse-labelled for 30 minutes with EdU, treated with DMSO or AZD1775 (600 nM) and chased for the times indicated. Mitotic status was analysed by labelling of phosphorylated S10-H3 at the indicated time points (Z-axes). Graphs represent the proportion of pS10-H3 positive cells.

Figure 4

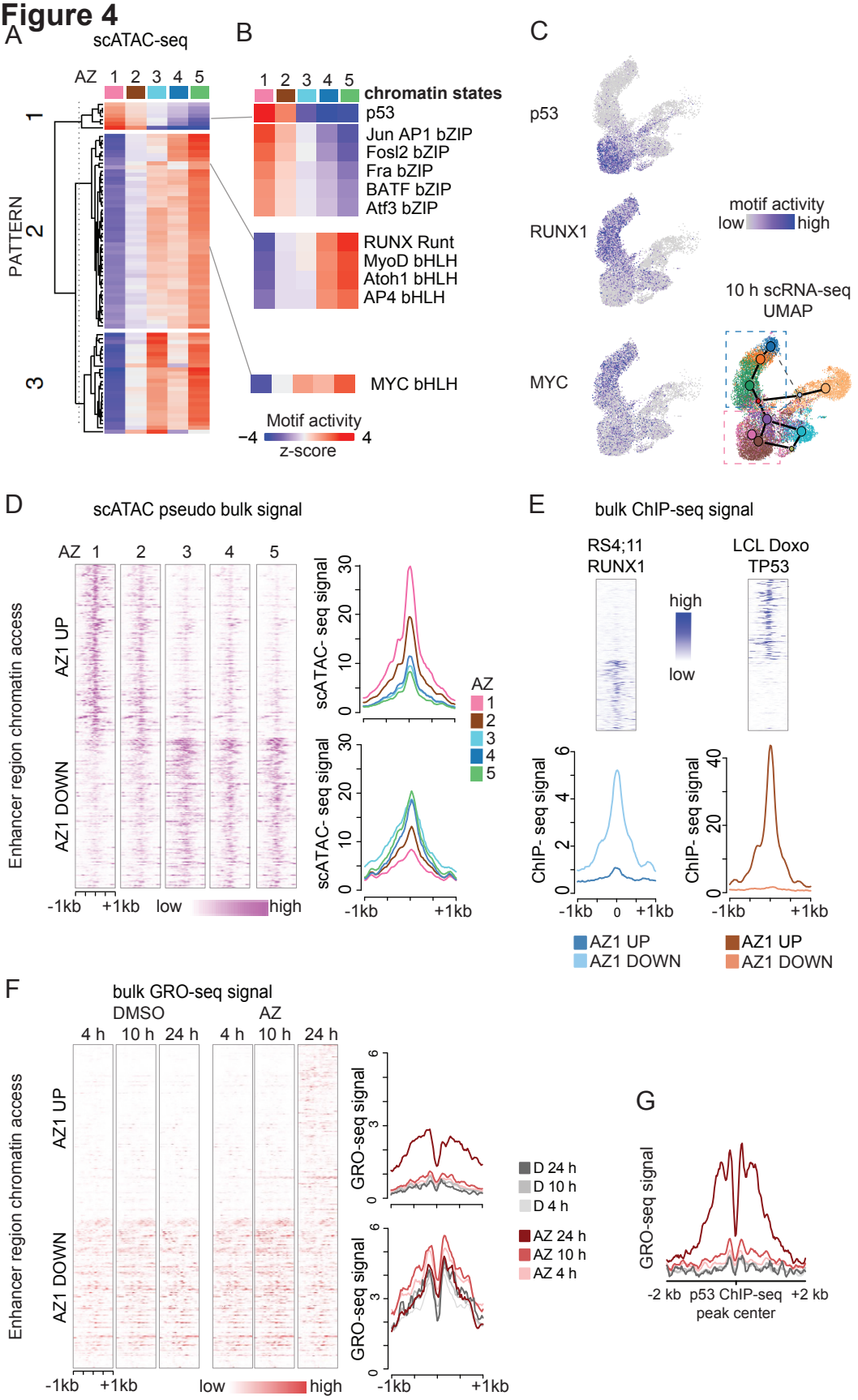
A
scATAC-seq
AZ 1 2 3 4 5
PATTERN
1
2
3
B
1 2 3 4 5
chromatin states
p53
Jun AP1 bZIP
Fosl2 bZIP
Fra bZIP
BATF bZIP
Atf3 bZIP
RUNX Runt
MyoD bHLH
Atoh1 bHLH
AP4 bHLH
MYC bHLH
Motif activity
−4
4
z-score
C
p53
RUNX1
MYC
motif activity
low
high
10 h scRNA-seq
UMAP
D
scATAC pseudo bulk signal
AZ 1 2 3 4 5
Enhancer region chromatin access
AZ1 UP
AZ1 DOWN
-1kb
+1kb
low
high
scATAC- seq signal
AZ
1
2
3
4
5
E
bulk ChIP-seq signal
RS4;11
RUNX1
LCL Doxo
TP53
high
low
ChIP- seq signal
-1kb
0
+1kb
AZ1 UP
AZ1 DOWN
F
bulk GRO-seq signal
DMSO
AZ
4 h
10 h
24 h
GRO-seq signal
D 24 h
D 10 h
D 4 h
AZ 24 h
AZ 10 h
AZ 4 h
G
-2 kb
p53 ChIP-seq
+2 kb
peak center

Figure 4. p53-driven gene regulatory response initiates from transcriptional silent chromatin and anti-correlates with RUNX1 binding.

A. TF motif activity across chromatin states 1-5 in 24 h AZD1775 treated sample is shown as a heatmap, where TF motifs (in rows) are clustered into three main patterns.

B. Pattern 1 TF motifs with highest motif access in cell fate II (top panel). Selected pattern 2 TFs are shown for comparison (bottom panel).

C. p53, RUNX1 and MYC TF motif activity shown on the UMAPs, as in Fig. 3A.

D. scATAC-seq signal at -/+ 1kb at 200 up- and downregulated enhancer regions most specific to AZD1775 chromatin state 1 vs other cell states. In the heatmap (left) each row corresponds to one enhancer and brighter color tones to higher access level. The magnitude and direction of changes in the cell state-specific chromatin accessibility signal across chromatin states 1-5 are summarized as average signal histograms (right).

E. ChIP-seq signal profile of RUNX1in RS4;11 cells (DMSO) and p53 from doxorubicin stimulated lymphoblastoid cells. TF occupancy signal heatmap and histogram at the same enhancer regions as shown in F.

F. GRO-seq signal heatmap and histogram at the same enhancer regions as shown in F.

G. GRO-seq signal histogram at ChIP-seq-based high-occupancy p53 binding sites is shown. Line color corresponds to treatment time and condition.

Figure 5

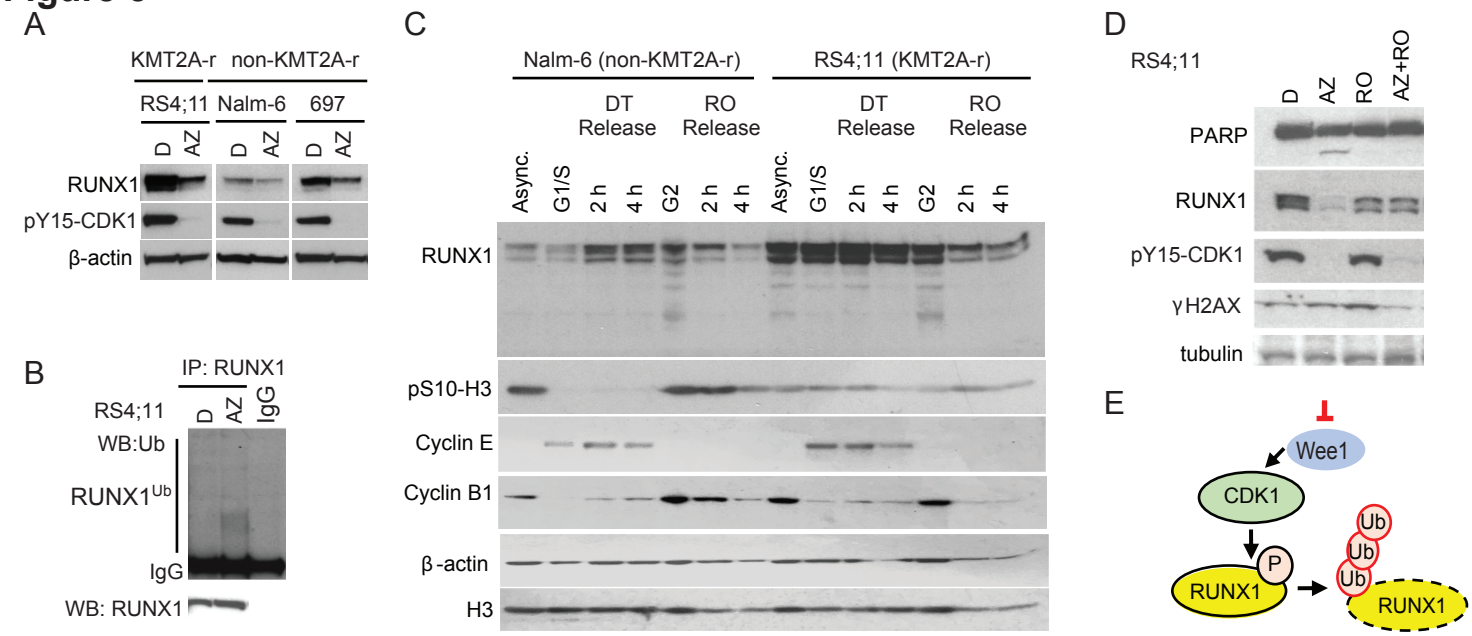
A
KMT2A-r
non-KMT2A-r
RS4;11
Nalm-6
697
D
AZ
D
AZ
D
AZ
RUNX1
pY15-CDK1
β-actin
B
IP: RUNX1
RS4;11
D
AZ
IgG
WB:Ub
RUNX1Ub
IgG
WB: RUNX1
C
Nalm-6 (non-KMT2A-r)
RS4;11 (KMT2A-r)
DT Release
RO Release
DT Release
RO Release
Async.
G1/S
2 h
4 h
G2
2 h
4 h
Async.
G1/S
2 h
4 h
G2
2 h
4 h
RUNX1
pS10-H3
Cyclin E
Cyclin B1
β-actin
H3
D
RS4;11
D
AZ
RO
AZ+RO
PARP
RUNX1
pY15-CDK1
γH2AX
tubulin
E
Wee1
CDK1
P
RUNX1
Ub
Ub
Ub
RUNX1

Figure 5. RUNX1 is degraded upon AZD1775-triggered CDK-activation.

A. RUNX1 protein levels in RS4;11, Nalm-6 and 697 treated with AZD1775 or DMSO for 24 h analysed by immunoblotting. Phosphorylation CDK1 was detected with pY15-CDK1 antibodies. β-actin is a loading control.

B. Treatment with AZD1775 promotes poly-ubiquitylation of endogenous RUNX1 in RS4;11 cells. Ubiquitylation assay was performed under denaturing condition to disrupt non-covalently linked ubiquitin. Ubiquitinated RUNX1 was detected by immunoprecipitation of endogenous RUNX1 followed by immunoblotting for ubiquitin after exposing cells to MG132. Expression of RUNX1 protein was examined in the whole-cell lysates.

C. RUNX1 protein expression in RS4;11 and Nalm-6 cells arrested at different cell cycle stages by double thymidine block (DT) or by treatment with RO3306 (RO) (CDK1 inhibitor). Asynchronous (Async) cells were treated with DMSO. Expression of cyclin E, cyclin B1 and phosphorylation of S10-H3 was analysed, as indicated. β-actin and H3 are loading controls.

D. RS4;11 cells treated with AZD1775, RO3306 or combination for 24h. Whole cell lysates were collected, and expression of RUNX1, cleaved PARP1, phosphorylation of CDK1-Y15 and phosphorylation of γH2AX-S139 analyzed by immunoblotting with the specified antibodies is shown. Tubulin is a loading control.

E. Schematic illustration of molecular mechanism linking CDK1 activity and RUNX1 protein degradation downstream WEE1 inhibition.

Figure 6

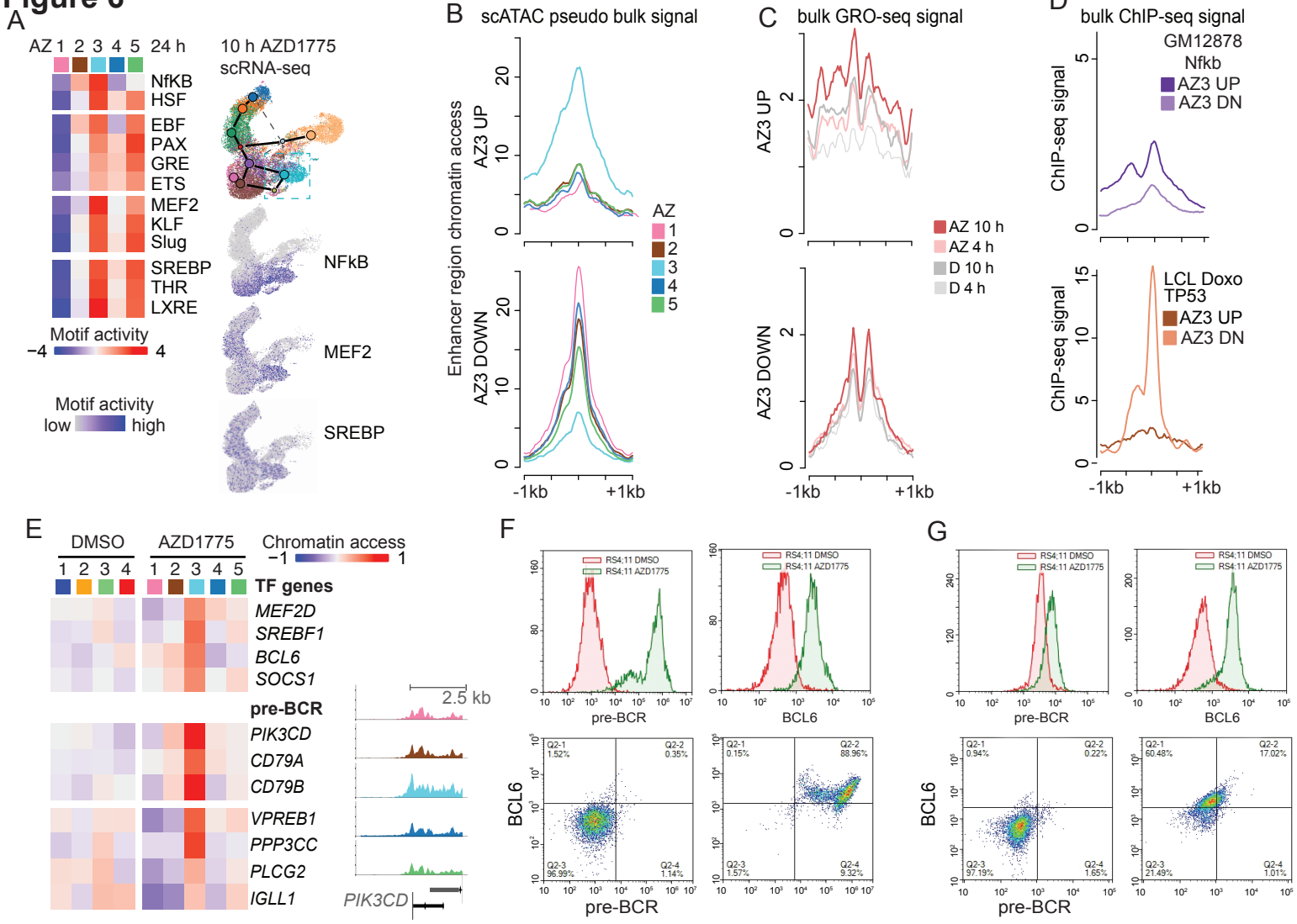
A
AZ 1 2 3 4 5 24 h
NfKB
HSF
EBF
PAX
GRE
ETS
MEF2
KLF
Slug
SREBP
THR
LXRE
Motif activity
−4 4
Motif activity
low high
10 h AZD1775
scRNA-seq
NFkB
MEF2
SREBP
B
scATAC pseudo bulk signal
Enhancer region chromatin access
AZ3 UP
AZ3 DOWN
AZ
1
2
3
4
5
-1kb
+1kb
C
bulk GRO-seq signal
AZ3 UP
AZ3 DOWN
AZ 10 h
AZ 4 h
D 10 h
D 4 h
D
bulk ChIP-seq signal
GM12878
Nfkb
AZ3 UP
AZ3 DN
ChIP-seq signal
LCL Doxo
TP53
AZ3 UP
AZ3 DN
E
DMSO
AZD1775
Chromatin access
−1 1
TF genes
MEF2D
SREBF1
BCL6
SOCS1
pre-BCR
PIK3CD
CD79A
CD79B
VPREB1
PPP3CC
PLCG2
IGLL1
2.5 kb
PIK3CD
F
RS4;11 DMSO
RS4;11 AZD1775
pre-BCR
BCL6
G
RS4;11 DMSO
RS4;11 AZD1775
pre-BCR
BCL6

Figure 6. Stress- and pre-B-state regulatory programs distinguish a drug-resistant sub-population with pre-BCR and BCL6 gene loci activation.

A. TF motif access across AZD1775 chromatin states is shown for TFs with high activity in cell fate III (Pattern 3, refer to Fig. 4A). Nf-KB, MEF2 and SREBP motif activity are visualized on the 10 h scRNA-seq UMAP.

B. scATAC-seq signal at -/+ 1kb at 200 up- and downregulated enhancer regions most specific to AZD1775 chromatin state 3 vs other cell states is shown as average signal histogram, as in Fig. 4D.

C. GRO-seq signal histogram at the same enhancer regions as shown in B.

D. ChIP-seq signal profile of NfKB in lymphoblastoid cells and p53 from doxorubicin stimulated lymphoblastoid cells. TF occupancy signal histogram is shown at the same enhancer regions as shown in B.

E. Chromatin access at TF and pre-BCR signaling related gene loci (gene body flanked by 2.5 kb up- and downstream) compared across AZD1775 chromatin states is shown as a heatmap (left). Aggregated scATAC-signal across cells assigned to each cluster is exemplified at *PIK3CD* gene region (right). The track colors correspond to 24 h AZD1775 chromatin state annotation.

F. Representative flow cytometry histograms and dot plots (lower panels) of pre-BCR receptor and BCL6 in RS4;11 cells treated with DMSO (red) and AZD1775 (600nM) (green) for 72 hours (F) followed by 10 days wash-out (G).

Figure 7

A *in vivo* MLL-7 scRNA-seq, AZD1775

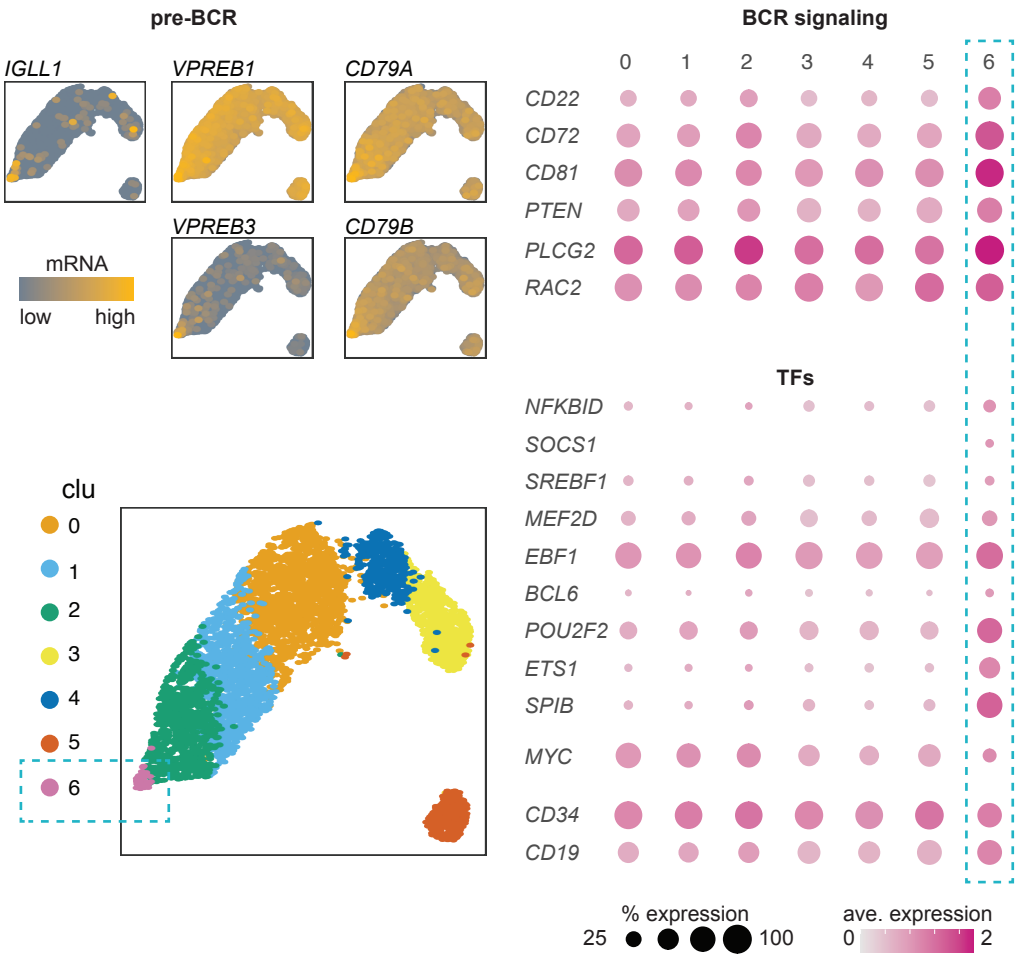

B ALL MEF2D, Day 2 blood scRNA-seq

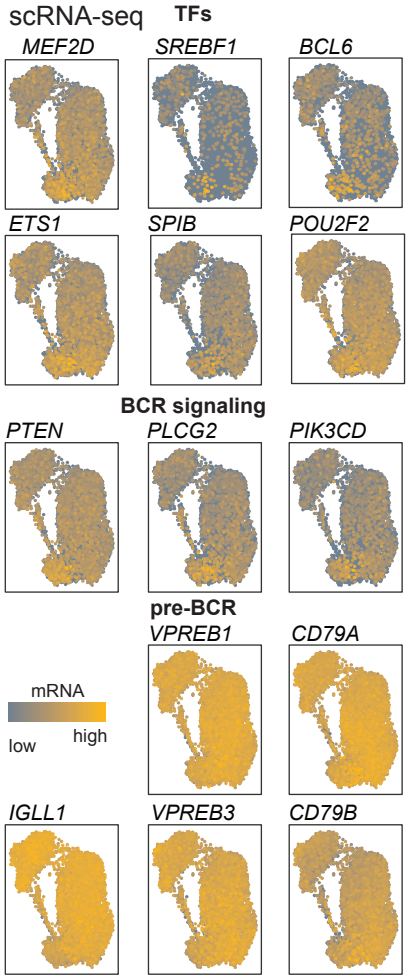

C Concurrent treatment

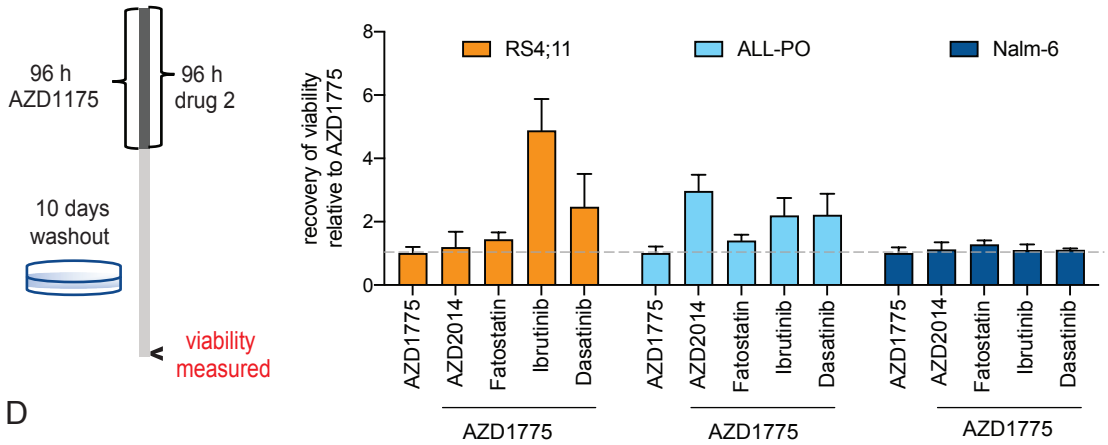

D Sequential treatment

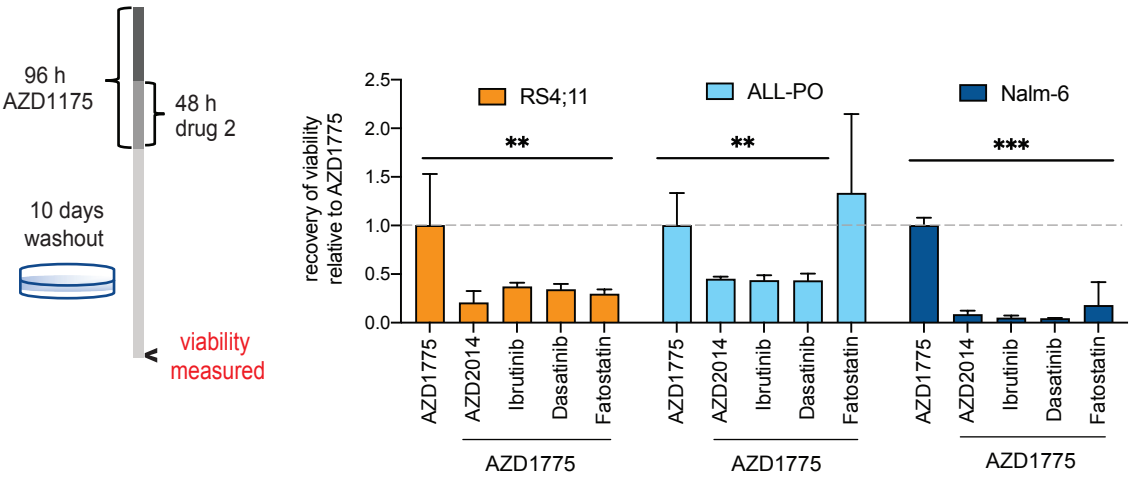

E

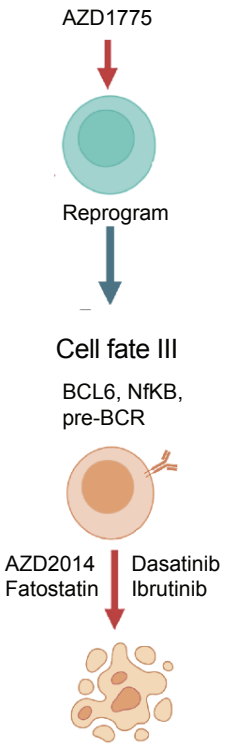

Figure 7. Sequential drug treatment targets drug-resistant cell state of leukemic cells

A. scRNA-seq transcriptome-based clustering for the primary MLL-7 cells treated with AZD1775 (24 h + 4 h) is shown on the UMAP visualization. Left panel top: mRNA level for pre-BCR genes visualized on the UMAP (brighter color tones correspond to higher level) bottom: colors correspond to cluster assignment. Right: dot plot heatmap shows BCR-signaling pathway related genes and pre-B cell fate TF genes. The percentage of cells expressing each gene is indicated by dot size and average expression level by tones of red.

B. scRNA-seq transcriptome-based clustering for the primary MEF2D-fusion ALL treated with standard chemotherapy. mRNA level is visualized on the UMAP as in A.

C. Left panel: overview of the experimental setup for concurrent drug treatment. Right panel: graph showing recovery of cell proliferation after concurrent treatment, following removal of AZD1775 with indicated drugs relative to recovery of cells treated AZD1775 alone. Cells were treated for four days with AZD1775 and indicated drugs and allowed to recover for an additional 10 days without the drugs. Regrowth was assessed using Alamar Blue stainings.

D. Left panel: overview of the experimental setup for sequential drug treatment. Right panel: Graph showing recovery of cell proliferation after sequential treatment, following removal of AZD1775 with drugs relative to cells treated with AZD1775 alone. Cells were treated for two days with AZD1775 following by co-culturing with indicated drugs for two days for 48h and allowed to recover for an additional 10 days without the drugs. Regrowth was assessed using Alamar Blue stainings. ** denotes $p<0.01$ and *** denotes $p<0.001$ between AZD1775 alone and indicated drug combinations determined using Student's t-test. Data are represented as mean ± SD.

E. Schematic model of the differential response to WEE1 inhibition in KMT2A-r leukemia.